



**HAL**  
open science

## Insights into Structures and dynamics of organic semiconductors through solid-state NMR spectroscopy

Martin Seifrid, G N Manjunatha Reddy, Bradley Chmelka, Guillermo Bazan

### ► To cite this version:

Martin Seifrid, G N Manjunatha Reddy, Bradley Chmelka, Guillermo Bazan. Insights into Structures and dynamics of organic semiconductors through solid-state NMR spectroscopy. *Nature Reviews Materials*, 2020, 5 (12), pp.910-930. 10.1038/s41578-020-00232-5 . hal-04102950

**HAL Id: hal-04102950**

**<https://hal.science/hal-04102950>**

Submitted on 22 May 2023

**HAL** is a multi-disciplinary open access archive for the deposit and dissemination of scientific research documents, whether they are published or not. The documents may come from teaching and research institutions in France or abroad, or from public or private research centers.

L'archive ouverte pluridisciplinaire **HAL**, est destinée au dépôt et à la diffusion de documents scientifiques de niveau recherche, publiés ou non, émanant des établissements d'enseignement et de recherche français ou étrangers, des laboratoires publics ou privés.

# Structures and Dynamics of Organic Semiconductors through Solid-State NMR Spectroscopy

Martin Seifrid,<sup>a</sup> G. N. Manjunatha Reddy,<sup>b\*</sup> Bradley F. Chmelka,<sup>c\*</sup> and Guillermo C. Bazan<sup>a,d\*</sup>

<sup>a</sup>*Center for Polymers and Organic Solids, Department of Chemistry and Biochemistry, University of California, Santa Barbara, California, 93106, U.S.A.*

<sup>b</sup>*Department of Chemistry, University of Lille, CNRS, Centrale Lille, Univ. Artois, UMR 8181-UCCS-Unité de Catalyse et Chimie du Solide, F-59000, France*

<sup>c</sup>*Department of Chemical Engineering, University of California, Santa Barbara, California, 93106, U.S.A.*

<sup>d</sup>*Departments of Chemistry and Chemical Engineering, National University of Singapore, Singapore, 117543.*

*Keywords: crystallinity, amorphous, disorder, thin films, OPV, OLED, OFET*

**ABSTRACT:** Organic semiconductors (OSCs) are of high fundamental and technological interest, because of their crucial properties and functions in a range of optoelectronic devices, including organic light-emitting diodes (OLEDs), organic photovoltaics (OPVs), and organic field-effect transistors (OFETs), as well as their promise in emerging technologies such as bioelectronic devices. The solid-state organization of the individual subunits in OSC materials, be they molecular or polymeric, determines the properties relevant to device performance, for example charge-carrier transport or optoelectronic behavior. Despite their importance, systematic composition-structure-processing-property relationships are rarely fully understood, due to the complexity of the organic architectures and the structures that result. Characterization of OSCs over different length- and time-scales is essential, especially for semi-ordered or amorphous regions for which solid-state nuclear magnetic resonance (ssNMR) spectroscopy yields important nanoscale insights that can be correlated with scattering and macroscopic property analyses. Here, we review selected recent results, challenges, and opportunities of ssNMR for OSC materials and summarize its role in state-of-the-art materials design and characterization. Examples are provided that illustrate how insight is obtained on local order and composition, interfacial structures, dynamics, interactions, and the establishment of structure-property relationships for high-performance OSC materials. Perspectives on applying ssNMR to the next-generation of OSC materials and the development of new ssNMR methods relevant to these objectives are also discussed.

## 1. Solid-state organic semiconducting materials

### 1.1. Significance of organic semiconductors in optoelectronics

Organic semiconductors (OSCs) have been a topic of extensive research in academic and industrial laboratories and are the basis of established and emerging technologies.<sup>1–3</sup> Indeed, although commercial organic light-emitting diodes (OLEDs) have become readily available to consumers,<sup>4</sup> research into materials with relevant photophysical features, for example thermally activated delayed fluorescence, continue to be at the forefront of research.<sup>5–8</sup> There are also significant ongoing efforts focused toward commercialization of other OSC technologies such as organic photovoltaic (OPV) devices and circuitry that rely on organic field-effect transistors (OFETs).<sup>9–11</sup> In addition, OSCs are promising materials for biological applications and bio-abiotic interfacing, such as neurological sensing and transformation of chemical signals to electronic signals, in devices such as organic electrochemical transistors (OECTs).<sup>12–22</sup> Their appeal as materials for future electronic devices is further evidenced by the success of neuromorphic computing devices based on OSCs.<sup>23,24</sup>

The extended  $\pi$ -conjugation and tunability of the chemical compositions and structures of OSCs are of paramount importance. Technologically relevant bulk properties, such as absorbance, luminescence, charge transport, band gaps, thermal stability or mechanical properties, are related to local and long-range organization in a material. Charge-carrier mobilities are heavily influenced by the electronic coupling between neighboring molecules, which in turn is determined by solid-state organization.<sup>25–27</sup> Control over material organization is mainly established at two levels: by molecular design and by processing conditions during film formation. Molecular composition and structure account for the various non-covalent interactions, such as  $\pi$ - $\pi$  stacking, van der Waals forces and hydrogen bonding, that ultimately direct intermolecular relationships.<sup>28,29</sup> The relatively weak nature of these interactions is also partly the reason for the appeal of OSCs as materials that can be processed under relatively mild conditions including from solutions, melts, or by vacuum thermal evaporation.

Many of the processing methods suitable for generating thin films provide kinetically stable morphologies, with degrees of order that span from single crystals to amorphous films.<sup>30–32</sup> It is important to distinguish well-ordered phases from regions with lesser degrees of order to correlate the local structures and processing dependences of an OSC with its macroscopic properties and the performance of associated devices.<sup>31</sup> Thin film morphologies are complicated and challenging to control because they evolve as individual “molecular” subunits self-organize during film formation. In the case of solution-processable OSCs, flexible alkyl groups are added as substituents on the conjugated backbone to achieve solubility.<sup>33–37</sup> The large degree of conformational disorder inherent in alkyl groups makes them effective solubilizing groups. However, they also discourage crystallization from solution during timescales typically associated with solvent evaporation. As a result, solution-processed OSC molecules and polymers may organize into different types of structures, which impact their bulk properties and ultimately technological viability.<sup>38</sup> Crystalline regions exhibit long-range structural order, while the amorphous phase contains no structural order, and semi-ordered domains exhibit intermediate extents of order. The presence, relative populations, and commingling of these different types of structures depend strongly on often-subtle details of OSC composition, architecture, and processing, which greatly influence the resulting material properties and device performance.

### 1.2. Characterization of OSC materials at different length scales

From the standpoint of establishing composition-structure-processing-property relationships, one must characterize and correlate OSC materials over molecular to bulk length scales. A particular challenge is the disorder often present as a result of the weak interactions that govern self-assembly of OSC materials, which leads to complex morphologies and structures that cannot be readily characterized at atomic resolution. X-ray scattering techniques can typically provide information on long-range, periodic structural order (10s to 100s of nm) in thin films that is due to  $\pi$ - $\pi$  (sub-nm) and lamellar (ca. a few nm) stacking.<sup>39</sup> However, such features are often accompanied by distributions of local environments and order that are manifested by broad scattering reflections, which are difficult to analyze in grazing incidence wide-angle X-ray scattering (GIWAXS) patterns. For example, it can be challenging to distinguish reflections associated with truly crystalline regions from those associated with partially crystalline regions, such as lamellar domains with  $\pi$ - $\pi$ -stacked backbones and disordered sidechains.<sup>38,40</sup> Neutron scattering is based on similar principles as X-ray scattering, but exploits the interactions of incident neutrons with nuclei (instead of incident X-rays interacting with electrons), and affords complementary information due to its sensitivity to chemical composition.<sup>41,42</sup> Electron microscopy is capable of imaging materials to atomic-scale resolution, though is best suited to robust materials with high degrees of order, which typically are not characteristic of OSCs.<sup>43-45</sup> Limitations associated with the scattering- and diffraction-based techniques described above are that they are generally insensitive to disordered (e.g., amorphous or dynamic) regions or moieties of a material, which can constitute an important fraction of OSC active layers that has been largely uncharacterized (FIG. 1a). Scanning probe microscopy techniques, such as scanning tunneling microscopy (STM) and atomic force microscopy (AFM), span the range of relevant length scales for OSC materials, from Ångströms (Å) to micrometers ( $\mu\text{m}$ ), and have proven to be useful for characterizing OSC materials.<sup>46,47</sup> However, these techniques are limited by the need for special sample preparation methods in cases where atomic resolution is desired, and by their restriction to probing only the surfaces of samples at larger length scales.

The sensitivity of solid-state NMR (ssNMR) spectroscopy to short-range interactions allows it to probe a wide array of material compositions, such as crystallites, lamellar mesophases and amorphous regions. The use of ssNMR techniques has therefore increased with the realization of its power to analyze complicated and heterogeneous material compositions, structures, and dynamics at an atomic scale.<sup>46,48-53</sup> In this context, ssNMR spectroscopy has emerged as an essential complementary tool, due to its compatible length (sub-nm) and time (ns-s) scales for *ex situ* and *in situ* characterization of short-range structures of complex soft materials (FIG. 1a). Moreover, ssNMR experiments can provide quantitative information on the composition of the entirety of a sample. As previously reviewed, early-stage developments of ssNMR spectroscopy for the study of conjugated materials were most often focused on doped molecular and polymeric conductors, such as polyacetylenes.<sup>54,55</sup> Over the past two decades, new technological advancements have enabled the investigation of complex heterogeneous OSC materials and their blends with unprecedented sensitivity and resolution.

The broad applicability and versatility of ssNMR spectroscopy is due the abundance of stable NMR-active nuclear isotopes and the different types of nuclear spin interactions that can be selectively probed in diverse inorganic, organic, and hybrid materials, including those with high extents of disorder or heterogeneity. The site-selectivity and short-range nature associated with different types of nuclear spin interactions enable local structures in ordered and disordered regions to be identified and distinguished. The sensitivity and resolution of ssNMR spectroscopy depends on the gyromagnetic ratio ( $\gamma$ ) and the abundance of NMR-active nuclear isotopes in the materials

under study. The choice of nuclei depends on the type of materials (for OSCs, typically  $^1\text{H}$ ,  $^{13}\text{C}$ ,  $^{15}\text{N}$  and  $^{19}\text{F}$ ), their natural isotopic abundance, and their spin. Although an in-depth discussion of ssNMR spectroscopy techniques is outside the scope of this review, there are several excellent books and reviews in the literature of basic concepts and applications<sup>56–59</sup> to which the reader is referred, as well as other works cited herein.

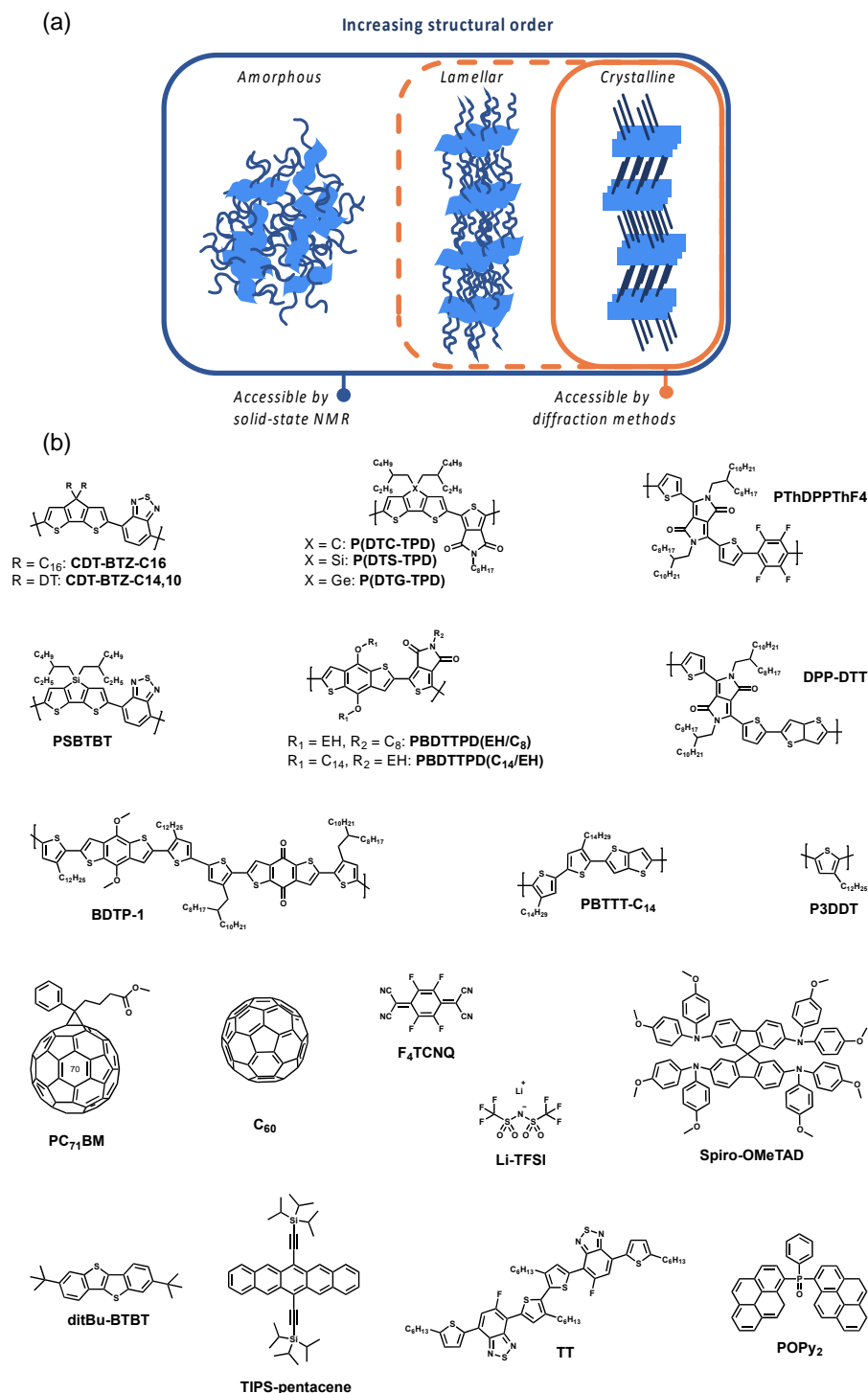


**Fig. 1** | (a) Schematic representation of the different degrees of order within OSC materials, and

*the sensitivity of ssNMR and diffraction-based methods to those regions. Compared to experimental methods such as X-ray, neutron or electron diffraction, ssNMR is capable of probing a broader range of structural and dynamical features of OSC materials, including disordered amorphous, lamellar mesophase, or highly crystalline regions. (b) Molecular structures of polymers and molecules discussed in the text that are not included in other figures are provided for reference.*

### 1.3. Complementarity of different analytical techniques and the multi-technique approach

As mentioned above, the composition and structure of semi-crystalline OSCs cannot be typically determined by scattering methods or microscopy techniques alone, and instead require a combination of complementary analytical techniques (FIG. 2). A multi-technique approach relies on protocols by which methods are combined to improve the effectiveness, accuracy, and completeness of the overall structure determination process. Modelling approaches based on density functional theory (DFT) calculations and molecular dynamics (MD) simulations have been used to bridge complementary experimental techniques, such as X-ray diffraction and ssNMR spectroscopy, so as to gain insights into how specific packing features and structures improve relevant properties.<sup>60,61</sup> Experimental techniques that validate structural models enable the determination of three-dimensional (3D) structures of OSC materials.<sup>62–68</sup> Such approaches are becoming increasingly popular owing to the ability to determine the structure of OSCs at complementary length scales (FIG. 2), for example using ssNMR spectroscopy (Å to nm), X-ray scattering (10s to 100s of nm) and electron microscopy (nm to μm). The underlying mechanisms of various optoelectronic processes can be studied by a range of optical spectroscopy techniques, however these methods provide little direct structural information.<sup>69,70</sup> To this end, the application of ssNMR spectroscopy for characterization of OSC materials has largely been centered on one-dimensional (1D) and two-dimensional (2D) techniques that provide important information on the local environments of each type of atom. Chemical shifts and dipole-dipole couplings are sensitive to differences in local bonding environments, conformations, inter- and intramolecular interactions. In addition, spin-diffusion analyses enable domain sizes to be determined with dimensions from a few nm to several 100s of nm. The use of pulsed-field gradient (PFG) NMR, which relies on the displacement of molecules or ions over length scales of 10-100 μm, enables molecular diffusivities to be determined in porous polymer networks.<sup>56</sup> The length scales associated with spin-diffusion and PFG NMR are complementary to morphological features characterized by AFM and STM. In addition to electronic structure and dynamics information, the frequency range associated with electron paramagnetic resonance (EPR) spectroscopy interactions and the accessible 1.5–8 nm distances from the radical centers could be attractive to characterize soft materials, as these length scales close a gap between distance information obtained from NMR spectroscopy and other long-range techniques.<sup>71–73</sup>

Furthermore, ssNMR techniques are sensitive to a wide range of timescales (ns to s) and can be used to probe various physicochemical, kinetic and thermodynamic processes such as photophysical processes (ns-μs), hydrogen bonding dynamics (~ns), molecular reorientations (ns-μs), aromatic ring flips, conformational rearrangements (μs-ms) and sidechain motions (ns-μs). Importantly, the sensitivity of ssNMR spectroscopy to short-range interactions is not predicated on the existence of medium- or long-range order. Correlating atomic-level structural and dynamical information obtained from ssNMR spectroscopy with scattering and macroscopic property analyses across multiple length (Å-μm) and time (ps-s) scales provides deep fundamental

insights on how chemical composition and processing influence structure and dynamics, and ultimately material and device performance.

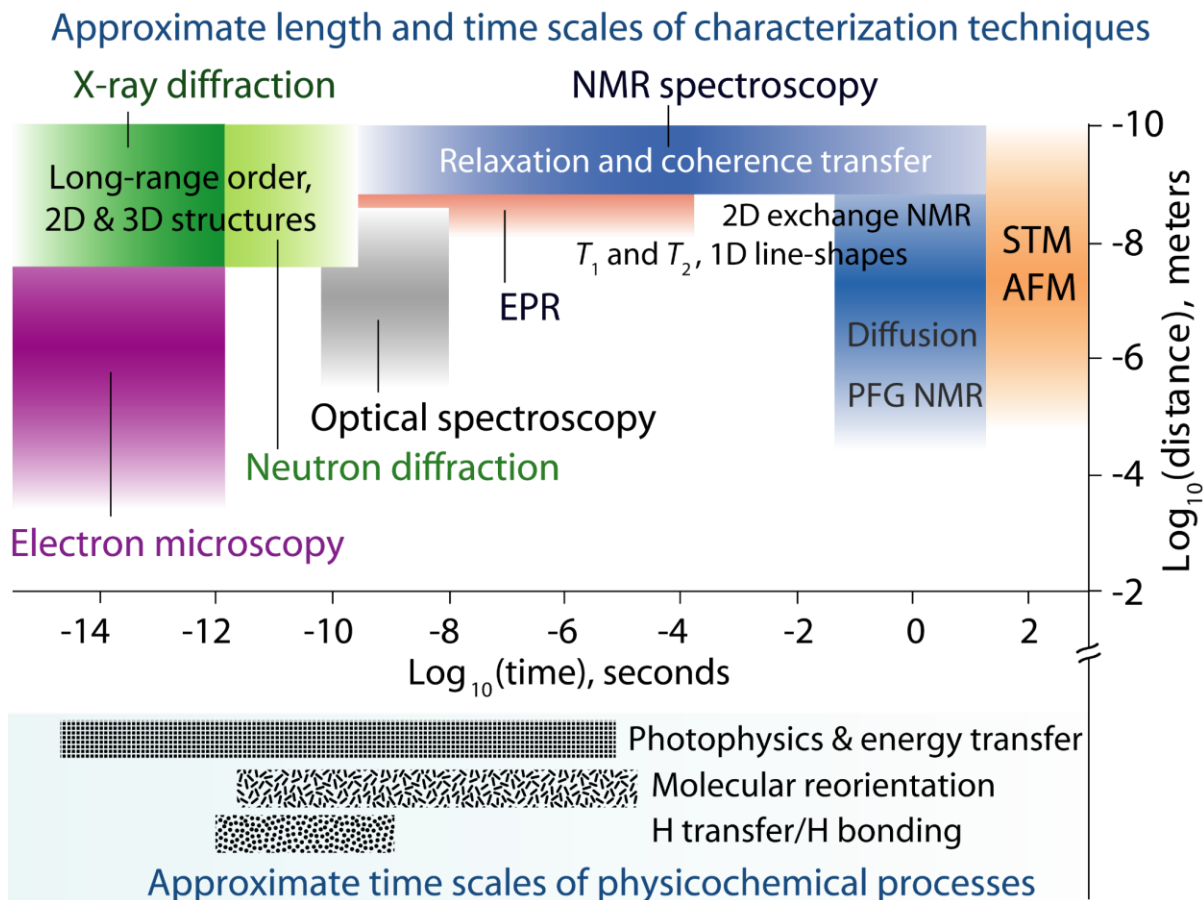


**Fig. 2** | (top) Approximate length and time scales of different characterization techniques used to analyze the structures and dynamics of OSC materials and thin films, compared with (bottom) the time scales of photophysical and dynamic processes. NMR spectroscopy probes short-range (nm) length scales and a broad range of timescales (ns-s), with the exception of spin-diffusion and PFG NMR measurements that extend the NMR length scales up to several 100s nm and 100s  $\mu\text{m}$ , respectively. Length and time scales are derived from guidelines in the literature, refs. 40, 41, 43, 46 and 74.

## 2. OSC composition and structure

### 2.1. Quantifying the degrees of order and disorder

The ability to identify and characterize short-range order is particularly important when relating different morphologies to charge carrier transport. The nanoscale sensitivity associated with ssNMR covers the entirety of OSC materials by enabling the local structures of ordered and disordered regions to be identified and distinguished. However, the quantitative information obtained from ssNMR depends on the length scales of interactions between adjacent nuclear spins. While the isotropic chemical shift is sensitive to the average bonding environments of atoms, other NMR interactions, such as chemical shift anisotropy, dipole-dipole interactions, quadrupolar interactions, Knight shifts, hyperfine interactions, or paramagnetic-induced interactions, can arise

from the proximities or relative orientations of different chemical moieties and the associated inter- and intramolecular interactions.<sup>54–59</sup> For example, anisotropic NMR interactions in solids often yield broad signals from distributions of chemically or structurally different sites that contain a wealth of structural and dynamics information, though, often complicate the analyses of heterogeneous soft materials.<sup>75</sup> Resolution of ssNMR signals can be enhanced by magic-angle-spinning (MAS), which involves rapid rotation of a sample in a specially designed rotor at an angle – the so-called “magic angle” (54.74°), relative to the static magnetic field ( $B_0$ ) to average out anisotropic interactions, or by applying homo- and heteronuclear decoupling sequences, or both. By comparison, inhomogeneous broadening of NMR signals cannot be easily narrowed, because it results from distributions of local environments such as found in glasses, amorphous polymers, or semicrystalline solids, that manifest intrinsic disorder within the material.

The isotropic chemical shift is the most readily accessible experimental parameter, and most often measured by conventional 1D MAS NMR experiments of spin  $\frac{1}{2}$  nuclei, such as  $^1\text{H}$ ,  $^{13}\text{C}$ ,  $^{15}\text{N}$ , and  $^{19}\text{F}$ . When sufficient resolution is attained in the 1D MAS NMR spectra, signals associated with ordered and disordered regions of OSC materials may be distinguished and quantified. For example, the  $^1\text{H}$  chemical shift is widely known to be sensitive to ring current effects,  $\pi$ - $\pi$ , CH- $\pi$  and hydrogen-bonding interactions. A  $^1\text{H}$  site centered above or below an adjacent aromatic ring experiences a large variation in the chemical shielding, due to CH- $\pi$  interactions, which leads to the displacement of a  $^1\text{H}$  signal towards a lower frequency. By comparison, a  $^1\text{H}$  site situated to the side of the aromatic ring leads to a  $^1\text{H}$  signal displacement toward higher frequency.<sup>20,21</sup> Isotropic  $^{13}\text{C}$  chemical shifts are reliable indicators of local chemical and structural environments, including conformation.<sup>76,77</sup> The  $\gamma$ -gauche effect (not to be confused with the gyromagnetic ratio) can be used to distinguish ordered and disordered sidechains. For example, when two methylene groups in an alkyl chain are in a  $\gamma$  position relative to one another and in *trans/trans* (*tt*) configurations, the isotropic  $^{13}\text{C}$  chemical shifts are displaced to higher frequencies, compared to otherwise identical alkyl chains in *trans/gauche* (*tg*) or *gauche/gauche* (*gg*) conformations, which are displaced to lower frequencies.<sup>77</sup> The analysis of different chemical shifts and lineshapes in an NMR spectrum can be used to quantify the degree of order and disorder within an OSC material. The degree of backbone crystallinity ( $X_c$ ) can be estimated from the integrated signal intensities of the crystalline ( $I_C$ ) and disordered ( $I_D$ ) fractions according to  $X_c = I_C / (I_D + I_C)$ .<sup>62</sup> It is noteworthy that the calculated degree of molecular order and disorder depends on the system and the analytical methods used.

Quantitative protocols to determine the degree of molecular order in semi-crystalline OSC polymers have been proposed by combining ssNMR analyses with X-ray scattering and computational modelling.<sup>49,62,78–81</sup> For example, in semi-crystalline regioregular poly(3-hexylthiophene) (P3HT), combined ssNMR spectroscopy, X-ray scattering and mass density calculations have suggested that there coexist (i) crystalline regions with long-range backbone and sidechain order, (ii) short-range order embedded in amorphous domains, and (iii) fully disordered regions.<sup>81,82</sup> Good agreement has also been demonstrated between the fraction of ordered P3HT chain segments estimated by  $^{13}\text{C}$  CP-MAS NMR experiments and by differential scanning calorimetry (DSC), once crystallite size is taken into account.<sup>79</sup> The degree of order observed in melt-annealed Form I P3HT, the polymorph most commonly found in devices, can be correlated to variations in molecular weight and processing conditions. For the comparison in **FIG. 3a**,  $^1\text{H}$  ssNMR measurements of Form I P3HT samples with molecular weights of 60 kg/mol (60k) and 25 kg/mol (25k) reveal 26% and 37% of the polymer chains to be ordered, respectively.<sup>62</sup> Wide-

angle X-ray scattering (WAXS) patterns of shorter (13 kg/mol, 13k) melt-annealed Form I P3HT chains indicate a crystalline contribution of 47%, while  $^{13}\text{C}$  ssNMR spectroscopy points to a greater proportion of crystalline regions (66%) due to its sensitivity to nanoscale domains invisible to X-ray scattering.<sup>82</sup> In the case of a spin-coated MEH-PPV film, integral deconvolution analysis of the 1D  $^{13}\text{C}$  NMR spectrum revealed that only a relatively low fraction (43%) of MEH-PPV backbones were locally ordered.<sup>83</sup>

A combination of ssNMR spectroscopy and MD simulations has been similarly used to distinguish crystalline, lamellar and amorphous regions based on local ordering in PBTTT backbones and sidechains (FIG. 3b).<sup>78</sup> Quantitation based on  $^1\text{H}$  and  $^{13}\text{C}$  ssNMR spectroscopies revealed a significant fraction (51%) of the PBTTT- $\text{C}_{16}$  backbones to be ordered. Analysis of the  $^1\text{H}$  NMR spectrum was used to differentiate and quantify the ordered and disordered  $\pi$ -conjugated backbones, while the  $^{13}\text{C}$  NMR spectrum was used to differentiate and quantify alkyl sidechains in the ordered *tt* conformation from those in the disordered *tg* or *gg* conformations. In conjunction with MD simulations, this information was used to determine that the powder composition of PBTTT- $\text{C}_{16}$  consists of 51% ordered (which includes 28% neat crystalline phase, 23% lamellar phase consisting of ordered backbones but disordered sidechains) and the remaining 49% consists of disordered backbones and disordered sidechains (amorphous phase). In contrast, PTB7-Th exhibits a much larger fraction (>99%) of locally ordered  $\pi$ -conjugated moieties as quantified by  $^{19}\text{F}$  ssNMR spectroscopy.<sup>83</sup> Since  $^{19}\text{F}$  nuclei are only present at one site of the PTB7-Th conjugated backbone, the short-range order determined here does not directly correlate to the overall degree of order in the backbone. This disparity is worth noting because PBTTTs are widely accepted as crystalline OSC materials. This difference can be attributed to the length scales that the two different techniques probe versus the domain sizes of the polymer aggregates; ssNMR methods take into account regions that are ordered within approximately 1 nm, even in the amorphous regions, whereas these contributions are invisible to X-ray scattering. It is important to note that these two methods of quantifying solid-state order are not exactly equivalent due to the sensitivity of the ssNMR method to highly local interactions. The short-range (~1 nm) nature of ssNMR spectroscopy provides a closer view of the compositional and structural heterogeneity in OSC materials. For example, ssNMR spectroscopy can identify backbones with a low degree of torsional disorder within the disordered regions. The decreased electronic disorder of these molecules may be correlated to the origin of “tie-chains” that have been identified in semi-crystalline OSC polymer films.<sup>84</sup>

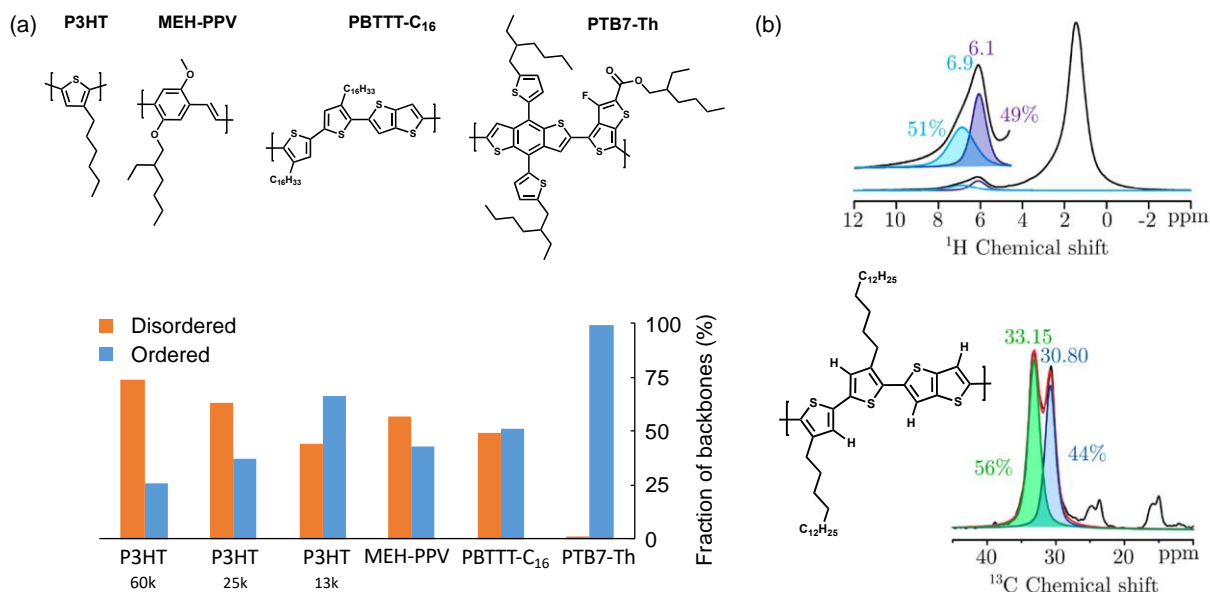


**Fig. 3** | (a) Histogram plot of relative fractions of locally ordered and disordered regions determined by ssNMR spectroscopy for different OSC materials with their schematic structures shown on top. (b) Schematic structure of PBT TT-C<sub>16</sub> with <sup>1</sup>H and <sup>13</sup>C ssNMR spectra which are sensitive to ordered and disordered regions. The <sup>1</sup>H spectrum shows intensities at 6.9 ppm and 6.1 ppm associated with disordered (51%) and π-π-stacked (49%) backbones that result in different local ring-current effects on the aromatic moieties. The <sup>13</sup>C spectrum resolves signals at 33.15 ppm and 30.80 ppm from alkyl sidechains in tt (56%) and tg/gg (44%) conformations that manifest different γ-gauche effects. Values for Figure 3a were taken from refs. 62, 78, 82, and 83. Figure 3b has been adapted from ref. 78.

The highly local nature of ssNMR spectroscopy can also result in overestimation of bulk crystallinity if the methods for quantification are not vigilantly compared. For example, in the histogram plot in FIG. 3a PTB7-Th is shown to have nearly uniformly ordered backbone structures. However, comparison of charge carrier mobilities between PTB7-Th and PBT TT reveals a more complex picture of the relationship between order and charge transport. In a diode device architecture, which measures charge transport through the bulk of a film, PTB7-Th and PBT TT exhibit hole mobilities of  $3.8 \times 10^{-4} \text{ cm}^2/\text{Vs}$  and  $1 \times 10^{-4} \text{ cm}^2/\text{Vs}$ , respectively.<sup>83,85</sup> However, PBT TT is primarily known as a very high mobility polymer in OFET architectures, where it has a hole mobility of up to  $1 \text{ cm}^2/\text{Vs}$ , a hundred-fold difference relative to PTB7-Th with a reported mobility of  $1.2 \times 10^{-2} \text{ cm}^2/\text{Vs}$ .<sup>86,87</sup> As such, it is important to take into account the sub-nm length scale investigated by ssNMR spectroscopy when correlating order with bulk properties, for instance, when long-range structural order is not a prerequisite for high-performance in OSC materials.

## 2.2. Determining packing interactions and 3D structures

Since heterogeneous OSC materials often do not exhibit long-range periodicity, efforts have been made to combine experimental techniques with computational modelling in order to determine the packing interactions in crystalline or semi-crystalline regions of OSCs (FIG. 4). In this pursuit, local structural constraints obtained by analyzing ssNMR spectra can be combined with structural information obtained from the X-ray scattering methods and analyses.

Homonuclear (e.g.,  $^1\text{H}$ - $^1\text{H}$ ) and heteronuclear (e.g.,  $^{13}\text{C}$ - $^1\text{H}$ ) dipole-dipole ( $D$ ) interactions, which originate from the interactions between neighboring nuclear spins and contain distance information, are useful for elucidating local structures of OSC materials. The effective strength of dipolar interactions depends on the factors including the gyromagnetic ratios and the natural isotopic abundances of the coupled nuclear spins, the separation distances, their orientations with respect to the external magnetic field ( $B_0$ ), and atomic or molecular mobilities in the material. 2D NMR spectra that correlate chemical shifts ( $\delta$ ) of different dipole-dipole coupled  $^1\text{H}$ - $^1\text{H}$  and  $^1\text{H}$ -X nuclei (X:  $^{19}\text{F}$ ,  $^{13}\text{C}$ ,  $^{14}\text{N}/^{15}\text{N}$ ,  $^{19}\text{F}$ ,  $^{29}\text{Si}$ , etc.) can be used to determine intermolecular proximities over nanoscale distances.

Several improvements have been sought to accelerate the structure-determination process, for example, by deriving local structural constraints from 2D homo- and heteronuclear correlation (HETCOR) NMR spectra. Such spectra also benefit from the sensitivity enhancement associated with polarization transfer from abundant nuclei (e.g.,  $^1\text{H}$  or  $^{19}\text{F}$ ) to less abundant nuclei (e.g.,  $^{13}\text{C}$  or  $^{15}\text{N}$ ) through dipole-dipole interactions, as exploited in cross polarization (CP) MAS experiments. The increase in sensitivity is proportional to the ratio of the respective nuclear gyromagnetic ratios, e.g.  $\gamma_{1\text{H}}/\gamma_{13\text{C}}$ .<sup>88</sup> Another means of enhancing spectral resolution is to apply a series of radiofrequency pulses to average homonuclear (e.g.,  $^1\text{H}$ - $^1\text{H}$ ,  $^{19}\text{F}$ - $^{19}\text{F}$ ) or heteronuclear (e.g.,  $^{13}\text{C}$ - $^1\text{H}$ ) dipole-dipole couplings, referred to as decoupling.<sup>89,90</sup> While the combination of MAS and decoupling techniques eliminates the dipole-dipole interactions, rotor-encoded 2D recoupling pulse sequences ensure the reintroduction of dipolar couplings to decode internuclear distance information in ssNMR spectra. To this end, 2D homonuclear double-quantum–single-quantum (DQ-SQ) correlation and CP-HETCOR experiments have been widely used to investigate OSC materials and their blends. When quadrupolar nuclei are involved, i.e. with nuclear spins  $I > 1/2$ , the nonspherical distribution of electric charge in the nucleus with its surrounding electric-field gradient dramatically influences lineshapes in the kHz to MHz range, resulting in quadrupolar couplings (Q) and quadrupolar induced shifts. In such cases, 2D multiple-quantum (MQ) MAS experiments aid the analyses of quadrupolar induced shifts and isotropic chemical shifts (FIG. 4).<sup>91–93</sup> Notably, 2D ssNMR in combination with electronic structure calculations provides site-specific information about structures and dynamics within complex OSC materials.<sup>62,67,78,94–100</sup> Local structural constraints obtained from NMR measurements and complementary analytical techniques such as X-ray scattering can be used as input parameters to the computation-based structure determination, whereby the number of conformational degrees of freedom are reduced to accelerate the overall structural determination process (FIG. 4).

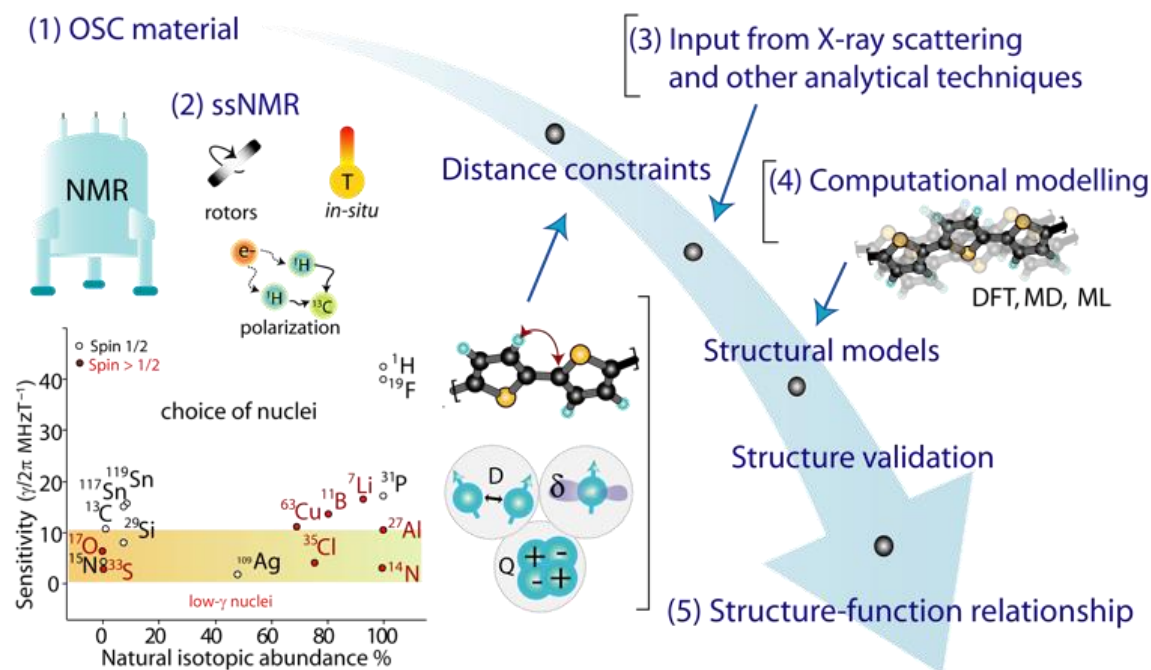


**Fig. 4** | Schematic diagram of integrated analyses of OSC materials using ssNMR spectroscopy coupled with computational modelling and complementary analytical techniques. An OSC material or thin film, packed into a rotor, can be analyzed using conventional and signal enhancement techniques for the detection of low-abundance nuclei such as  $^{13}\text{C}$  and  $^{15}\text{N}$ , which can be achieved by different spin polarization transfer techniques discussed in the below sections. Short-range structures and interactions characterized by means of chemical shifts and dipole-dipole couplings are combined with X-ray scattering analysis. Information on local chemical environments (e.g. distance constraints) together with input on long-range order from complementary techniques and computational modelling are used to validate structural models, which help elucidate structure-function relationships in OSC materials. This figure will be used as a point of reference through the remainder of the text.

**Light emitting diodes (OLEDs).** Understanding the molecular-level origins of different emission wavelengths and optical properties of OLEDs has long been a topic of interest.<sup>92,101–106</sup> Blue- and green-emitting tris(8-hydroxyquinoline) aluminum(III) ( $\text{Alq}_3$ ) complexes have isomeric structures with different emission wavelengths and quantum yields.<sup>101</sup> The facial (fac) and meridional (mer) forms of  $\text{Alq}_3$ , owing to different conformations of the ligands, are anticipated to exhibit different emission wavelengths,<sup>92,102,104,105</sup> or different intermolecular interactions are assumed to also contribute to different emission wavelengths.<sup>103,106</sup> While  $\text{Alq}_3$  meridional isomers in the  $\alpha$ - and  $\beta$ -polymorphs emit green light, the blue-emitting  $\gamma$ - and  $\delta$ -polymorphs of  $\text{Alq}_3$  are the facial isomers.<sup>107,108</sup> Reaching a consensus regarding the atomic-level origins of these different optical properties is challenging since films of  $\text{Alq}_3$  often exist as a mixture of different crystalline and amorphous forms.<sup>92,93</sup> In this context,  $^{13}\text{C}$  and  $^{27}\text{Al}$  ssNMR spectroscopy in conjunction with DFT calculations has been used as a complementary tool to elucidate inter- and intramolecular interactions in different crystalline  $\text{Alq}_3$  polymorphs, as well as amorphous  $\text{Alq}_3$ .<sup>93,109–111</sup> Quadrupolar interactions characterized by  $^1\text{H}$ -decoupled 2D  $^{27}\text{Al}\{^{27}\text{Al}\}$  MQ MAS NMR have shown the presence of relatively well-ordered  $^{27}\text{Al}$  sites in facial isomers ( $\gamma$  and  $\delta$  polymorphs), as compared to the less ordered  $^{27}\text{Al}$  sites in a meridional isomer ( $\alpha$  polymorph) and the amorphous

phase. While the amorphous phase consists of Alq<sub>3</sub> molecules with locally disordered aluminum sites, the  $\alpha$  polymorph exhibits two distinct locally ordered structures, distinguished by the <sup>27</sup>Al isotropic chemical shifts of the  $\alpha_1$  (31 ppm) and  $\alpha_2$  (30.5 ppm) polymorphs (cyan arrows, FIG. 5a), and amorphous Alq<sub>3</sub> (a broad distribution of signals centered at 30.5 ppm, red arrow, FIG. 5a) obtained from the analyses of 2D <sup>27</sup>Al{<sup>27</sup>Al} MQMAS NMR spectra (FIG. 5a). The ssNMR results and analyses thus provide insight, at least in part, into the different optoelectronic properties associated with Alq<sub>3</sub> isomers that are often obtained as a mixture containing a distribution of different crystalline polymorphs and amorphous regions.<sup>92,93</sup>

*Field effect transistors (OFETs).* The impact of molecular structure on solid-state organization and charge transport in OFETs has been elucidated using ssNMR spectroscopy, X-ray scattering and computational modelling.<sup>94,96,97,112</sup> Of particular interest are the CDT-BTZ polymers (FIG. 1b), differing only in the structure of their sidechains, which showed marked differences in their charge carrier mobilities. The well  $\pi$ - $\pi$  stacked backbones of CDT-BTZ polymers with linear hexadecyl (C<sub>16</sub>) alkyl chains (CDT-BTZ-C16) exhibited superior mobilities as compared to the branched 2-decyltetradecyl (DT) alkyl sidechains (CDT-BTZ-C14,10). By employing 2D <sup>13</sup>C{<sup>1</sup>H} and <sup>1</sup>H{<sup>1</sup>H} MAS NMR spectroscopy, X-ray scattering and DFT calculations, it was determined that polymers with branched alkyl chains exhibited larger  $\pi$ -stacking distances caused by a lateral shift of the backbones.<sup>96,97</sup> It is noteworthy that the modest (1-2 Å) longitudinal shift of the conjugated backbones can be related to significant differences in electronic structure. In addition, modelling approaches have identified lamellar structures with interdigitated alkyl chains that differ by the relative orientation of the side groups with respect to the CDT-BTZ backbone. These subtle structural differences were also corroborated by comparing the simulated GIWAXS patterns and NMR chemical shifts as a function of the relative position of the polymer chains with those obtained from experimental GIWAXS and ssNMR results. Similar methods have been used to shed light on the effects of subtle structural changes on the charge carrier properties of isoindigo-based polymers, as well as the poly(cyclopentadithiophene-*alt*-thienopyrrolodione) polymers P(DTC-TPD), P(DTS-TPD) and P(DTG-TPD) that incorporate group 14 atoms (FIG. 1b, C in DTC, Si in DTS and Ge in DTG, respectively).<sup>100,113</sup> <sup>1</sup>H MAS NMR experiments have been used to distinguish between the *syn* and *anti*-conformers, indicating that *anti*-conformation is preferred between the DTS/DTG and TPD moieties in P(DTS-TPD) and P(DTG-TPD), while P(DTC-TPD) does not exhibit a preference toward a particular conformer. These results are corroborated by the 2D <sup>1</sup>H{<sup>1</sup>H} DQ-SQ NMR experiments, which provide evidence for aromatic-aromatic correlations in P(DTS-TPD) and P(DTG-TPD) that are absent from P(DTC-TPD), indicating strong differences in the backbone  $\pi$ - $\pi$  stacking arrangements between P(DTC-TPD) and polymers with silicon or germanium bridgehead atoms, P(DTS-TPD) and P(DTG-TPD). Recently, ssNMR has been used to understand the impact of thermal annealing on the structure of a polymer, PThDPPThF4 (FIG. 1b), which exhibits charge transport properties similar to those of a single crystal.<sup>112</sup> *Ex situ* 2D <sup>19</sup>F{<sup>19</sup>F} DQ-SQ NMR experiments revealed that thermally annealed films obtained from the melting endotherm temperature results in a slip-stacked packing arrangement in which the electron-poor diketopyrrolo-pyrrole (DPP) and tetrafluorobenzene (F4) units in one chain  $\pi$ - $\pi$  stack with the electron-rich thiophene (Th) units of neighboring chains. Specifically, the three pairs of cross-correlation intensities in the 2D <sup>19</sup>F{<sup>19</sup>F} DQ-SQ NMR spectrum suggest the presence of two distinct packing modes in which the polymer chains are slipped in different directions relative to one another.

Where thin films of ~100s nm in thickness are involved, the acquisition of ssNMR spectra becomes challenging and often requires much longer experimental times. In addition to conventional CP-MAS signal enhancement techniques, dynamic nuclear polarization (DNP) NMR techniques have been developed to exploit the much higher intrinsic polarization associated with the transfer of microwave-irradiated paramagnetic electron spins to nuclear spins.<sup>114-117</sup> DNP NMR can theoretically yield signal enhancements according to the ratio  $\gamma_e/\gamma_n$ , where  $\gamma_e$  and  $\gamma_n$  are the respective gyromagnetic ratios of the electron and nuclear spins, which lead to theoretical sensitivity enhancements of up to ~660, ~2600, and ~6600 for  $^1\text{H}$ ,  $^{13}\text{C}$ , and  $^{15}\text{N}$  nuclei, respectively. Sensitivity gains depend on material composition, the type of polarizing radical, solvent, temperature, microwave power and magnetic field strength. A combined DFT and 2D  $^{13}\text{C}\{^1\text{H}\}$  DNP surface-enhanced NMR spectroscopy (SENS) approach has enabled the determination of diketopyrrolo-pyrrole-dithienylthieno[3,2-b]thiophene (DPP-DTT, structure shown in **FIG. 1b**) packing interactions in bulk material and drop-cast 440 nm thick films, revealing that the polymer adopts a highly planar backbone conformation with a slip-stacked donor-on-acceptor arrangement.<sup>67</sup>

*Photovoltaic materials and blends.* Combined NMR, X-ray scattering and DFT modelling efforts are also of relevance to OPV research.<sup>62,67,78,95,98,99</sup> Unit-cell parameters and space groups derived from X-ray scattering experiments have been combined with spatial constraints obtained from 2D ssNMR techniques to facilitate *in silico* verification of specific packing models in different structures obtained from quantum-chemical studies, as described in **FIG. 4**. In such strategies, interatomic distances have been measured by analyzing  $^1\text{H}$ - $^1\text{H}$ ,  $^{13}\text{C}$ - $^1\text{H}$ ,  $^{13}\text{C}$ - $^{13}\text{C}$  and  $^{13}\text{C}$ - $^2\text{H}$  dipole-dipole couplings, and used as structural constraints to build molecular packing models. Examples include the 3D structure determination of semi-crystalline P3HT polymers with different molecular weights.<sup>62,99</sup> Additionally, information on domain sizes can be obtained by employing dipolar-mediated spin-diffusion ssNMR spectroscopy which is sensitive to magnetization exchange between dipole-dipole coupled spins.<sup>118-120</sup> A proof-of-concept that exploits spin-diffusion NMR, and high-resolution optical and electron microscopy has been used to probe P3HT:PCBM materials, providing an estimate of ~3 nm for the sizes of the domains with an average of two neighboring P3HT chains around each PCBM molecule.<sup>81,120</sup>

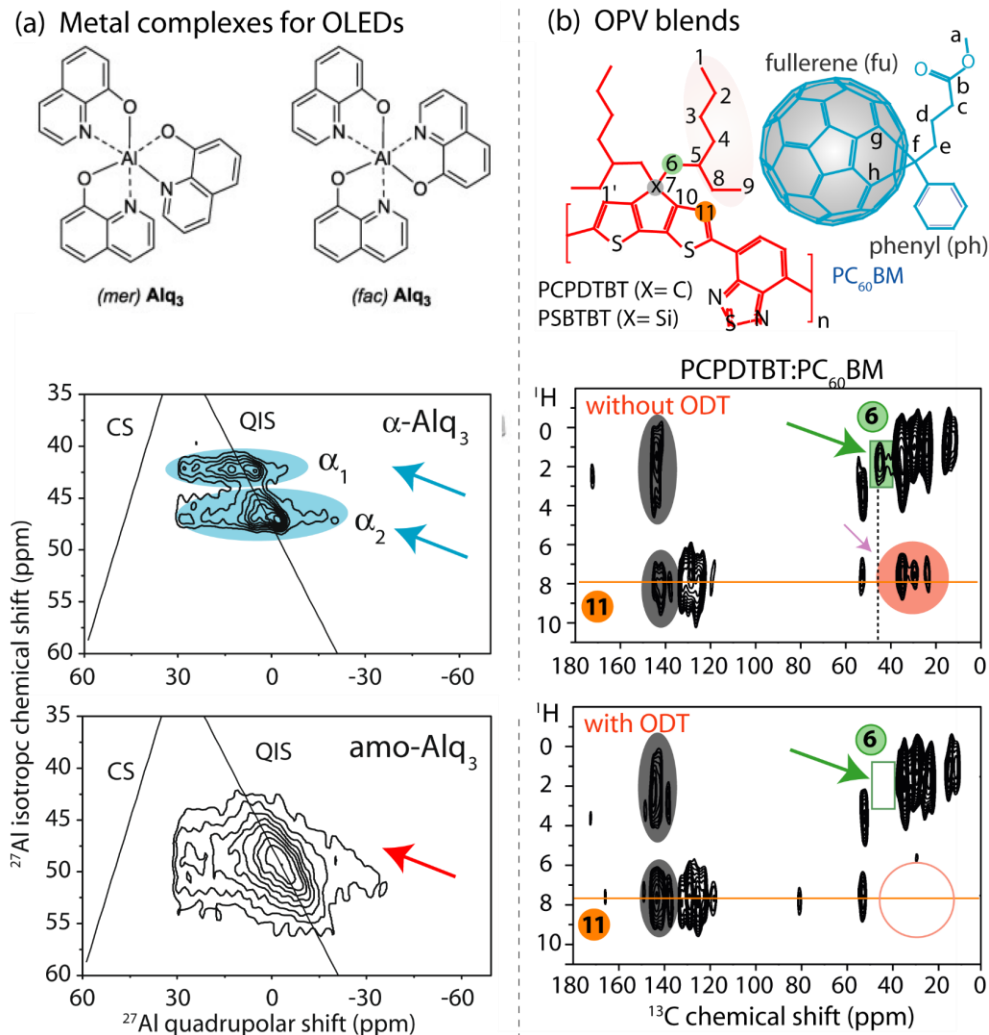


**Fig. 5** | (a) 2D  $^{27}\text{Al}\{^{27}\text{Al}\}$  MQMAS NMR spectra of the  $\alpha$  polymorph (top) and amorphous  $\text{Alq}_3$  (bottom). (b) Solid-state  $^{13}\text{C}\{^1\text{H}\}$  NMR spectra of PCPDTBT:PCBM blends, in which the correlated intensities shown manifest  $^1\text{H}$ - $^{13}\text{C}$  nanoscale proximities associated with the influence of the solvent additive ODT on intermolecular interactions at the donor-acceptor interface. Figure 5a has been adapted from ref. 93. Figure 5b has been adapted from ref. 121.

### 2.3. Characterization of interfacial structures

Further complexities in structural organization are present in multicomponent systems, such as in the case of blends or molecular dopants. Blends of two or more OSC materials include donor-acceptor bulk heterojunction (BHJ) photoactive layers,<sup>122</sup> ternary and quaternary BHJ blends,<sup>123</sup> and small-molecule doped OSCs for OFET and OLED applications.<sup>124–126</sup> The BHJ concept is a milestone in the design of high-performance OPV materials that has promoted extraordinary activity in the search for new donor and acceptor materials and ways to optimize blend compositions and morphologies.<sup>37,127,128</sup> Molecular dopants may be added to alter the energy levels of the host material in order to modify charge transport, or to act as emitters.<sup>129–131</sup> Since charge transport in OSC blends is governed by intermolecular electronic coupling, controlling molecular packing, interfaces and thin-film morphology is essential to attain high efficiency and device-to-device reproducibility. Much remains to be known about the structural details of interfaces,

particularly across different length scales (FIG. 2).

**Bulk heterojunctions.** During film formation, differences in chemical structure result in phase separation and development of the BHJ morphology. The resulting interfaces play a critical role in the performance of an OPV device.<sup>132–137</sup> Differences in intermolecular contacts between donor polymers and fullerenes result in major differences in electron delocalization, charge separation and power conversion efficiency (PCE).<sup>138,136</sup> Due to the inherently low volume fraction relative to bulk material, and the disorder of the donor-acceptor interface, it remains a challenge to probe this critical region of the active layer. Examples of ssNMR-based studies for establishing the structure of donor-acceptor interfaces include BHJ blends such as P3HT:PC<sub>61</sub>BM, PBDTTPD:PC<sub>61</sub>BM, PSBTBT:PC<sub>61</sub>BM, PBTTT:PC<sub>71</sub>BM and BDTP-1:C<sub>60</sub> blends (molecular structures in FIG. 1b).<sup>139–143</sup> Donor-acceptor interfacial contacts in fullerene docking with the family of benzo[1,2-b:4,5-b']dithiophene-thieno[3,4-c]pyrrole-4,6-dione polymer (PBDTTPD) derivatives (2-ethylhexyl/octyl, EH/C<sub>8</sub> and tetradecyl/2-ethylhexyl, C<sub>14</sub>/EH) have been elucidated using 2D <sup>1</sup>H{<sup>13</sup>C} ssNMR spectroscopy.<sup>139</sup> Device efficiencies of the different blends show that contact between the fullerene and the electron-deficient TPD unit, promoted by steric hindrance from the branched EH alkyl chain on the benzodithiophene (BDT) moiety, improves charge generation and PCE.<sup>139</sup> In 2D <sup>1</sup>H{<sup>13</sup>C} ssNMR spectra of these blends, intensity correlations between the <sup>13</sup>C signals associated with the PC<sub>61</sub>BM acceptor and <sup>1</sup>H signals of the EH/C<sub>8</sub> donor are reliable indicators to infer the close spatial proximities (<1 nm) that are required for efficient charge transfer in BHJs. Similar 2D <sup>13</sup>C{<sup>1</sup>H} HETCOR NMR techniques have been employed along with WAXS measurements and MD simulations to gain insight into the interfacial interactions in a PBTTT-C<sub>16</sub>:PC<sub>71</sub>BM bimolecular crystal (molecular structure shown in FIG. 1b).<sup>140</sup> Analysis of 2D ssNMR spectra of BHJ blends serves as the basis to understand interfacial contacts. Comparison of 2D spectral maps of neat compounds versus blends enables direct correlation of the displacement of chemical shifts and lineshapes to molecular order.

2D ssNMR spectroscopy has also been used in conjunction with transient absorption pump–probe spectroscopy to correlate structure with charge transport in PCPDTBT:PC<sub>60</sub>BM BHJ blends processed from different solvents.<sup>121,144</sup> The impact of solvent on the nanoscale structures can be realized by directly comparing the 2D <sup>13</sup>C{<sup>1</sup>H} HETCOR spectrum of PCPDTBT:PC<sub>60</sub>BM drop-cast from *ortho*-dichlorobenzene (*o*-DCB) to that of the same material processed with 2.44% by volume of the solvent additive octanedithiol (ODT).<sup>121</sup> Solvents additives, such as ODT, increase drying time and allow BHJ blends to adopt morphologies more favorable to optimal device performance.<sup>145–149</sup> A comparison of 2D <sup>13</sup>C{<sup>1</sup>H} HETCOR spectra of PCPDTBT:PC<sub>60</sub>BM processed with and without ODT (FIG. 5b) shows obvious differences in the correlation intensities. The presence and absence of the 2D correlation intensity corresponding to the methylene group (C6) next to the bridgehead carbon atom (<sup>13</sup>C, ~45 ppm and <sup>1</sup>H, 1.7 ppm) of the EH side chains in the 2D spectrum (green arrows, FIG. 5b) is suggestive of the changes in the arrangement of the side chains in PCPDTBT:PC<sub>60</sub>BM processed without and with ODT, respectively. Changes in the sidechain arrangements in PCPDTBT:PC<sub>60</sub>BM were also evidenced by the 2D <sup>13</sup>C{<sup>1</sup>H} correlation intensities (<sup>13</sup>C, 20–40 ppm and <sup>1</sup>H, ~7.9 ppm) depicted by hollow and filled circles in FIG. 5b. A similar 2D HETCOR spectrum of a drop-cast PSBTBT:PC<sub>60</sub>BM blend, which differs only in replacement of the carbon bridging atom with a silicon in the polymer's donor moiety, showed relatively narrow <sup>13</sup>C linewidths corresponding to the highest average local ordering, even in the absence of ODT.<sup>121</sup> These examples illustrate the suitability of ssNMR as an atomic-level technique to probe the differences in sidechain organization.

**Molecularly-doped OSC materials.** Recent studies have focused on providing insight into intermolecular interactions in doped conducting polymers.<sup>150–152</sup> ssNMR has been applied to analyze OSCs doped with 2,3,5,6-tetrafluoro-7,7,8,8-tetracyanoquinodimethane (F<sub>4</sub>TCNQ, shown in FIG. 1b). Electrical conductivities ranging from 0.1 S cm<sup>-1</sup> to 22 S cm<sup>-1</sup> can be obtained upon doping P3HT with F<sub>4</sub>TCNQ using different processing conditions.<sup>153,154</sup> Another example is the semi-crystalline polymer PBTTT-C<sub>14</sub> (FIG. 1b), which can be doped by F<sub>4</sub>TCNQ, due to a favorable energetic offset between the ionization energy of PBTTT-C<sub>14</sub> and the electron affinity of F<sub>4</sub>TCNQ, allowing charge transfer in solutions and in thin films.<sup>155–159</sup> Analyses of a combination of 1D <sup>19</sup>F and 2D <sup>1</sup>H{<sup>13</sup>C} ssNMR spectra of PBTTT-C<sub>14</sub>:F<sub>4</sub>TCNQ films at molar ratios of 0.075 and 0.25 provide crucial insights into the co-facial arrangement of F<sub>4</sub>TCNQ and PBTTT-C<sub>14</sub>, where charge transfer can be 100% efficient in the solid state.<sup>151</sup>

To provide an example of in-depth ssNMR characterization of molecularly-doped OSCs, the delineation of binding properties of the Lewis acid tris(pentafluorophenyl)borane (BCF) to the polymer PFPT and the mechanisms of bandgap engineering in PFPT:BCF thin films have been corroborated by 1D and 2D ssNMR spectroscopy.<sup>152</sup> Spatially-resolved maps of interfacial contacts in PFPT:BCF thin films were realized by analyzing the 1D <sup>11</sup>B, <sup>13</sup>C{<sup>1</sup>H} and <sup>13</sup>C{<sup>19</sup>F} CP-MAS NMR spectra, and 2D <sup>1</sup>H{<sup>19</sup>F} and <sup>1</sup>H{<sup>1</sup>H} correlation NMR spectra (FIG. 6). While the 1D <sup>11</sup>B MAS NMR spectrum of a 1:1 PFPT:BCF complex exhibits a signal at -1.8 ppm (FIG. 6a) that is characteristic of tetrahedrally-coordinated boron atoms, a comparison of the 1D <sup>13</sup>C{<sup>1</sup>H} and <sup>13</sup>C{<sup>19</sup>F} CP-MAS NMR spectra (FIG. 6b,c) allowed <sup>13</sup>C signals with different intensities, associated with different BCF and PFPT moieties, to be distinguished. The partially-resolved signals at 123 ppm and 129 ppm correspond to the aromatic carbon atoms color coded in the schematic figure (green, red, cyan, and purple) that are directly bonded to protons in fluorene moieties. The relatively narrow <sup>13</sup>C signal at 153 ppm is assigned to the six carbon atoms (grey) of the PFPT moieties. By comparison, the 1D <sup>13</sup>C{<sup>19</sup>F} CP-MAS spectrum shows <sup>13</sup>C signals (145-150 ppm and 132-138 ppm) enhanced by <sup>19</sup>F nuclei that are directly bonded to the carbon atoms (black) in the BCF moieties. Of particular interest, the <sup>13</sup>C signal at 123 ppm associated with the carbon atom (green) adjacent to the pyridyl nitrogen in the pyridylthiadiazole moiety is also relatively enhanced by <sup>19</sup>F spin-polarization, which indicates its proximity to the fluorine atoms in BCF. Next, intensity correlations in the 2D <sup>1</sup>H{<sup>19</sup>F} heteronuclear multiple quantum coherence (HMQC) NMR spectrum (FIG. 6e) between <sup>1</sup>H signals at 8.2 ppm (aromatic groups of PFPT) and 1.1 ppm (branched alkyl sidechains of PFPT) with the <sup>19</sup>F signals at -163 ppm and -158 ppm from the *meta* and *para* BCF fluorines establish the close spatial proximities of these PFPT and pentafluorophenyl (C<sub>6</sub>F<sub>5</sub>) moieties. In contrast, no correlated intensity is observed between aromatic <sup>1</sup>H signals of PFPT and the *ortho* <sup>19</sup>F signal of C<sub>6</sub>F<sub>5</sub> moieties (-133 ppm), reflecting weaker <sup>19</sup>F-<sup>1</sup>H dipole-dipole interactions with the PFPT backbone and sidechain <sup>1</sup>H sites. In the <sup>1</sup>H DQ-SQ correlation spectrum (FIG. 6d), the off-diagonal intensity correlations at <sup>1</sup>H SQ chemical shifts of 1.1 ppm and 8.2 ppm, and at <sup>1</sup>H DQ chemical shift of 1.1 + 8.2 = 9.3 ppm are due to intramolecular proximities of the C<sub>16</sub> alkyl chains and aromatic fluorene moieties of PFPT, but not between the sidechain and thiadiazolopyridine groups of PFPT. These 1D and 2D NMR analyses are consistent with the formation of a polymer:Lewis acid adduct in which BCF molecules bind near the pyridyl nitrogen atoms of PFPT. Such methods can be easily extended to study the binding properties of various molecular dopants incorporated in OSC materials.

Application of ssNMR spectroscopy goes beyond identification of short-range interactions, for instance by offering intimate details on the doping mechanisms. For example, <sup>7</sup>Li MAS NMR spectroscopy has been used to uncover the roles of lithium bis(trifluoromethylsulfonyl)-imide (Li-

TFSI) in 2,20,7,70-tetrakis(N,N-di-p-methoxyphenylamine)9,90-spirobifluorene (Spiro-OMeTAD) based solid-state dye-sensitized solar cells by comparing the spectra of neat Li-TFSI, doped Li-TFSI:Spiro-OMeTAD (molecular structures in FIG. 1b) and the oxidized product of Li-TFSI:Spiro-OMeTAD (upon exposure to air over 12 h).<sup>150</sup> The results of these studies proposed a doping mechanism that is triggered by consumption of the Li<sup>+</sup> ions during device operation. Such a finding is troublesome because the concentration of Li<sup>+</sup> is required to be maintained at approximately 20 mol% with respect to Spiro-OMeTAD for optimal device performance.<sup>150</sup>

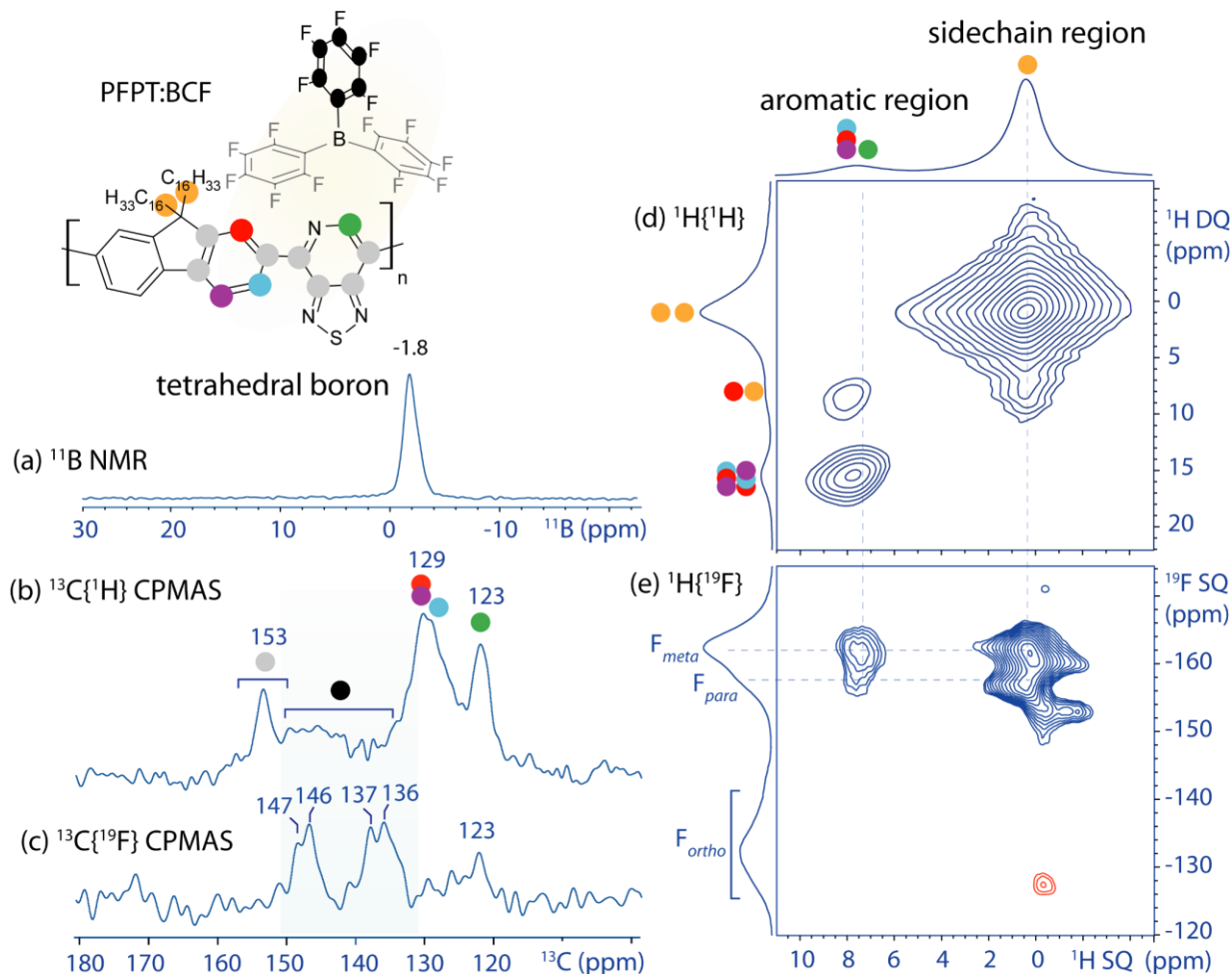


**Fig. 6** (a)  $^{11}\text{B}$ , (b)  $^{13}\text{C}\{^1\text{H}\}$ , (c)  $^{13}\text{C}\{^{19}\text{F}\}$ , (d)  $2\text{D } ^1\text{H}\{^1\text{H}\}$ , and (e)  $^1\text{H}\{^{19}\text{F}\}$  ssNMR spectra for elucidating spatial proximities in the Lewis basic semiconducting polymer PFPT, doped by BCF (schematic structure). Figure 6 has been adapted from ref. 152.

### 3. Dynamics in OSC materials

Molecular motions occur in OSC materials at different timescales (ps-ms) due to fluctuations in local structures, aromatic ring flips, rotational dynamics of flexible alkyl groups, free rotations around sigma bonds, and exchange of hydrogen atoms.<sup>160</sup> Since rotational and vibrational motions (FIG. 2) occur at much shorter timescales than those of both ssNMR (ms-s) and diffraction experiments (s-min), both of these techniques lead to inherently time-averaged structures. It is noteworthy in this context that the dipole-dipole interactions are proportional to the internuclear

distance  $r^{-3}$ , and so the relevant time-averaged parameter for NMR is  $r^{-3}$  rather than the typical  $r$  dependence for Bragg diffraction. It is, however, difficult to measure molecular motions in amorphous regions of OSC materials using X-ray diffraction methods due to the lack of periodic order. ssNMR observables are sensitive to site-selective dynamics at much shorter timescales (FIG. 2) such that the impact of dynamic processes is less disruptive. In particular, motional averaging of specific functional groups, such as rapidly rotating methyl groups or phenyl ring flips, can lead to partially averaged anisotropic interactions and improved resolution, thereby enabling site-specific dynamics of molecular entities to be measured and distinguished.<sup>56</sup> Nuclear spin relaxation processes, such as spin-lattice ( $T_1$ ) or spin-spin ( $T_2$ ) relaxation, influence lineshapes, which can be used to elucidate dynamics associated with the backbones and sidechains of OSCs.<sup>81,160–164</sup>

### 3.1. Phase transitions and molecular motion

The timescales associated with NMR spectroscopy facilitate the measurement of several dynamic processes in OSC materials: (i) “fast” dynamics associated with molecular rotations (i.e. rotational correlation times) and phenyl ring flips can be determined through temperature-dependent relaxation rates, and can be related to activation energies; (ii) chemical exchange between different sites, which is characteristic of NMR lineshapes;<sup>56</sup> and (iii) slow dynamics involving breaking of bonds or significant structural rearrangement.<sup>48,49</sup> Analysis of fast-slow limits can be attained by measuring the signal full-width-at-half-maximum (FWHM) as a function of temperature, which provides insight into the nature of the dynamic process. Similar ssNMR techniques, together with optical microscopy, single-crystal X-ray diffraction, DSC and Raman spectroscopy, have been applied to investigate the molecular origin of cooperative phase transitions in molecular crystals.<sup>165</sup> It was found that rotational disorder of the bulky side chains in 2,7-di-*tert*-butyl[1]benzothieno[3,2-*b*]benzothiophene (ditBu-BTBT) and 6,13-bis(triisopropylsilylethynyl)pentacene (TIPS-pentacene) (molecular structures in FIG. 1b) can be used as a molecular design tool to control cooperative changes in molecular packing.

Recent work employing the study of nuclear spin relaxation rates, so-called ssNMR relaxometry, has helped to elucidate the impact of molecular structure on site-specific dynamics and phase properties.<sup>161–163</sup> Previous studies have shown that the temperature-dependent  $^{13}\text{C}$  spin-lattice relaxation rates ( $R_1$ ) associated with different  $^{13}\text{C}$  sites (FIG. 7a) provide site-specific dynamics information about the backbones and sidechains of poly(3-alkylthiophene) (P3AT) derivatives, and were able to determine activation energies ( $E_a$ ) for the motion of the alkyl groups.<sup>161,162</sup> A comparison of  $^{13}\text{C}$  relaxation rates of the  $\text{C}_{16}$  sidechains below and above 230 K suggests an inhomogeneous-to-homogeneous transition, i.e., crystal (C) to plastic crystal (PC), upon heating. The authors suggest that at approximately 240 K the accelerated sidechain motions trigger the thiophene ring twist, leading to a PC state. At 300 K, a transition to a regime of extremely narrow relaxation rates indicates that rapid alkyl group motion occurs in the PC state. Above 300 K, molecular motions associated with the sidechain and thiophene groups both enter into the narrow regime, which leads to decreased  $R_1$ . Activation energies of the motion of the alkyl groups, as determined from ssNMR measurements that exhibited non-Arrhenius behavior, were found to be 6.5-8.2 kJ/mol (below 240 K), 18.0-22.0 kJ/mol (240-270 K) and 24.8-29.7 kJ/mol (above 310 K). In short, dynamic processes determined from temperature-dependent ssNMR measurements are consistent with thermodynamic phase diagrams constructed using DSC, variable temperature UV-vis and infrared spectroscopy measurements (FIG. 7b). In another study,  $^1\text{H}$  and  $^{13}\text{C}$   $T_1$  relaxation measurements of neat P3HT and P3HT:PCBM BHJ blends were used to

understand their dynamic behaviors, which showed different morphologies and phase properties before and after thermal annealing at 150 °C.<sup>163</sup>

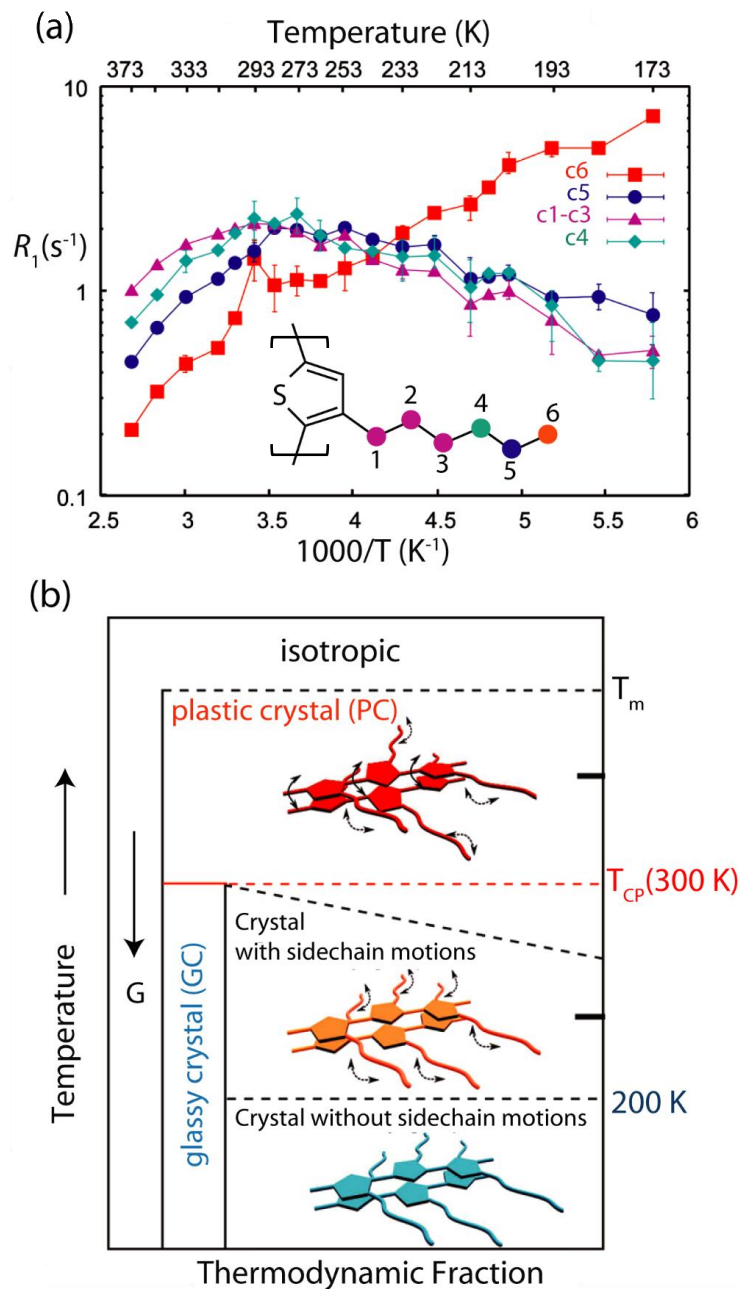


**Fig. 7** | (a) Temperature-dependent <sup>13</sup>C spin-lattice relaxation rates  $R_1$  for alkyl sidechains. (b) Proposed phase diagram for P3AT derivatives, with the horizontal axis depicting the fraction of phases and non-equilibrium states estimated by FTIR measurements. Figure 7 has been adapted from ref. 162.

The interplay between different dynamic processes associated with backbone and sidechain motions has been inspected by correlating  $T_1$  relaxation rates with MD simulations in model P3AT derivatives.<sup>164</sup> The faster motions associated with longer sidechains accelerate thiophene ring fluctuations. MD simulations corroborate these results by showing that the motion of poly(3-

dodecylthiophene-2-5-diyl) (P3DDT, **FIG. 1b**) backbones occurs at a relatively faster timescale than those of P3HT – a feature attributed to the presence of longer sidechains in P3DDT. A recent study further corroborates this idea by showing the differences in the dynamic behavior of two different P3HT films obtained from different drying conditions using X-ray scattering, DSC and  $^{13}\text{C}$  ssNMR spectroscopy measurements.<sup>81</sup> The study showed that the thiophene  $^{13}\text{C}$  NMR peak widths are broadened at temperatures lower than 273 K, whereas at temperatures higher than 273 K narrower thiophene resonances are observed because of the faster side chain motions that accelerate the thiophene ring fluctuations. The thiophene conformational rearrangements occur on time scales in the range of subms-to-ms ( $\ll 3$  ms) such that the P3HT backbones are conformationally disordered at ambient temperature,<sup>81</sup> which is consistent with the glassy crystal phase, GC, shown in **FIG. 7b**.<sup>162</sup>

### 3.2. Dynamics of film formation

There are significant changes in bulk properties, such as optical absorption, during phase transitions that can be related to changes in local structures and dynamics. Understanding both intra- and supramolecular organization during phase transitions, such as thermal annealing, crystallization and solid-to-solution transformation would be beneficial for further refinements of molecular design principles. In this respect, an understanding of changes in molecular shape, as well as inter- and intramolecular interactions, can be attained by ssNMR spectroscopy techniques. The application of *in situ* and *ex situ* ssNMR methods is particularly relevant to examine the evolution of molecular order at heterogeneous OSC interfaces. *In situ* and *ex situ* ssNMR techniques have previously been conceived to monitor phase transitions between complex crystalline phases, labile supramolecular assemblies, or to “view” structural changes in molecular self-assembly upon liquid-to-solid phase transitions.<sup>166–173</sup> For example, a bithiophene derivative (TT, **FIG. 1b**), which exhibits unusual behavior during its transition to the solid state, has been shown to undergo changes in its molecular topology during crystallization.<sup>174,175</sup> *In situ*  $^{13}\text{C}$  ssNMR experiments combined with DFT calculations have been employed to ascertain that TT initially forms an amorphous glass, which slowly transitions into a crystalline film while at the same time the molecule adopts a planar conformation. This *in situ* NMR study provided unequivocal information about site-specific differences in  $^{13}\text{C}$  frequencies observed for the planar and twisted molecular topologies. Similarly, DNP-enhanced ssNMR spectroscopy has been applied to the orientational analysis of OSC thin films.<sup>176</sup> The relative orientation of P=O bonds in vacuum-deposited and drop-cast phenyldi(pyren-1-yl)phosphine oxide (POPy<sub>2</sub>, **FIG. 1b**) were shown to exhibit anisotropic and isotropic distributions of POPy<sub>2</sub> moieties on substrates, respectively, thus revealing a molecular origin for differences in charge transport properties. These studies emphasize how information on local structure and dynamics obtained from ssNMR spectroscopy can be used to understand how local structures impact macroscopic properties.

## 4. Conclusions and future perspectives

Compositional and structural heterogeneity in OSC materials makes it challenging to develop structure-processing-property relationships by using a narrow range of characterization techniques. The subnano- to nanoscale sensitivity associated with ssNMR interactions enables distinct local environments and inter- and intra-molecular interactions to be distinguished and identified. ssNMR spectroscopy results and analyses are best used when supported by complementary experimental techniques and modelling approaches. Such insights have been

seldom available for inherently complex heterogeneous OSC materials and their blends. In addition, ssNMR is well-suited to measurement of dynamics on these length and time scales. This review gives particular attention to recent advancements in the development and application of ssNMR for OSC materials, whose findings have important implications for understanding the roles of inter- and intramolecular interactions and dynamics in solid-state organization, morphology, phase transitions and bulk optoelectronic properties.

More recently developed OSC technologies, such as OECTs and neuromorphic computing chips, will require development of novel materials that couple electronic and ionic charge transport. The presence of a solvent or additives in these devices introduces yet another layer of complexity to an already multifactorial system. Indeed, as many studies have revealed, crystallinity and long-range structural order are not a critical requisite.<sup>84</sup> Instead, locally ordered backbones may be a general feature for achieving high performance in OSC-based optoelectronic devices.<sup>84,177–179</sup> Undoubtedly, the complementary structural and dynamics information obtained from NMR spectroscopy can be combined with additional experimental and computational methods so as to establish structure-property relationships in OSC materials with complex architectures. Inspiration can be taken from previous efforts to understand the synergy between local structures and dynamics of ionic transport in systems such as batteries, supercapacitors<sup>180–182</sup> and conjugated- or metal-organic frameworks (COFs and MOFs),<sup>183–186</sup> as well as biological macromolecules.<sup>187–189</sup>

Ultra-high magnetic field spectrometers in combination with very fast MAS rates are anticipated to enable acquisition of high-resolution ssNMR spectra of OSC thin films at sub-milligram quantities. Furthermore, signal enhancements obtained by DNP NMR spectroscopy are providing new insights into the structures of surfaces and interfaces,<sup>114–116</sup> though they have been so far rarely applied to OSCs.<sup>67,176,190</sup> While these developments offer a promising future, the sensitivity and resolution of ssNMR will be challenged by the complexity of OSC materials. Examples of such complex materials include ternary and quaternary BHJ blends,<sup>123</sup> as well as conjugated oligoelectrolytes (COE) and polyelectrolytes (CPE) interacting with biological systems for use in medical and bioelectronics applications.<sup>16,191–195</sup> There remains the need to develop ssNMR techniques with even greater sensitivity and resolution to detect the low- $\gamma$  quadrupolar isotopes (FIG. 4) present in OSC devices, such as <sup>14</sup>N, <sup>17</sup>O, <sup>33</sup>S, <sup>43</sup>Ca, <sup>115</sup>In, <sup>117/119</sup>Sn and <sup>197</sup>Au.<sup>196</sup> Analyses of ssNMR spectra of these nuclei is expected to help characterize the interfaces between OSC active layers, interlayers and electrodes at atomic-level resolution. However, acquisition of the NMR spectra of these nuclei is challenging because of their low natural isotopic abundance (an order magnitude lower than  $\gamma$  of <sup>1</sup>H) and large quadrupolar interactions (up to several MHz). Ultra-high magnetic fields (>25 T) in conjunction with improved probe technologies (e.g., MAS >150 kHz with sub-mm rotors or spheres)<sup>197,198</sup> are expected to enhance the sensitivity and resolution in ssNMR spectra of OSCs. Advancements in ssNMR experiments for the selective detection of local domains,<sup>68,199</sup> as well as new detection techniques,<sup>200</sup> can potentially be used to selectively probe specific nuclei in OSC materials and thin films.

Characterization of materials in working OSC devices at an atomistic level of detail provides yet another opportunity and formidable challenge, as it relates to understanding device function and stability. Further development of integrated analysis workflows incorporating ssNMR spectroscopy, as depicted in FIG. 4, will improve our understanding of a broader range of OSC materials. Advancements in ssNMR spectroscopy, such as ultra-high magnetic field spectrometers and DNP-NMR mentioned earlier, coupled with sample preparation methods using fast MAS

rotors or spheres, and *in situ* experimental conditions will enable the determination of local structural constraints. Chemical shift-based 3D structure determination to verify structural models obtained through computational models from DFT or MD depends on the ability to calculate them using high quality first-principles calculations. To this end, the accuracy of chemical shift calculations using advanced plane-wave DFT approaches (gauge including projector augmented waves, GIPAW) and machine-learning (ML) algorithms have been compared.<sup>201</sup> Such methods are yet to be developed and applied for complex organic polymers. However, the ML-based ShiftML, which has been shown to predict chemical shifts within DFT accuracy at much lower computational cost, has the potential to overcome the costs associated with quantum chemical calculations of large organic molecules. Structural models derived from ssNMR and computational modelling can then be validated with input from the complementary experimental techniques discussed earlier. Integration of the methods described above will result in improvements in the understanding of structure-processing-property relationships, and in important advancements in the molecular design of OSCs.

### **Acknowledgements**

The authors acknowledge funding support from the Department of the Navy, Office of Naval Research, Award Nos. N00014-14-1-0580 and N00014-16-1-2520 and the Mitsubishi Chemical Center for Advanced Materials (MC-CAM). G.N.M.R. gratefully acknowledges the European Union's Horizon 2020 research and innovation program under the Marie Skłodowska-Curie Award No. 795091. We thank Prof. M. R. Hansen for helpful discussions and for providing us with ssNMR spectra.

### **Author contributions**

M.S. and G.N.M.R. researched the literature and wrote the initial manuscript draft. All authors contributed to discussion of the content and edited the different drafts before submission.

### **Competing interests**

The authors declare no competing interests.

### **ORCID**

Martin Seifrid: 0000-0001-5238-0058

G. N. Manjunatha Reddy: 0000-0002-8283-2462

Bradley F. Chmelka: 0000-0002-4450-6949

Guillermo C. Bazan: 0000-0002-2537-0310

### **References**

1. Brédas, J.-L. & Marder, S. R. *The WSPC Reference on Organic Electronics: Organic Semiconductors: Volume 1: Basic Concepts*. vol. 1 (WORLD SCIENTIFIC, 2016).

2. *Organic electronics. 1: Materials, manufacturing and applications.* (Wiley-VCH, 2008).
3. *Organic Electronics II: More Materials and Applications.* (Wiley-VCH Verlag GmbH & Co. KGaA, 2012).
4. Oh, C.-H. *et al.* 21.1: Invited Paper: Technological Progress and Commercialization of OLED TV. *SID Symp. Dig. Tech. Pap.* **44**, 239–242 (2013).
5. Adachi, C. Third-generation organic electroluminescence materials. *Jpn. J. Appl. Phys.* **53**, 060101 (2014).
6. Di, D. *et al.* High-performance light-emitting diodes based on carbene-metal-amides. *Science* **356**, 159–163 (2017).
7. Liu, Y., Li, C., Ren, Z., Yan, S. & Bryce, M. R. All-organic thermally activated delayed fluorescence materials for organic light-emitting diodes. *Nat. Rev. Mater.* **3**, 18020 (2018).
8. Hamze, R. *et al.* Eliminating nonradiative decay in Cu(I) emitters: 99% quantum efficiency and microsecond lifetime. *Science* **363**, 601–606 (2019).
9. Krebs, F. C., Espinosa, N., Hösel, M., Søndergaard, R. R. & Jørgensen, M. 25th Anniversary Article: Rise to Power - OPV-Based Solar Parks. *Adv. Mater.* **26**, 29–39 (2014).
10. Min, J. *et al.* Evaluation of Electron Donor Materials for Solution-Processed Organic Solar Cells via a Novel Figure of Merit. *Adv. Energy Mater.* **7**, 1700465 (2017).
11. Guo, X. *et al.* Current Status and Opportunities of Organic Thin-Film Transistor Technologies. *IEEE Trans. Electron Devices* **64**, 1906–1921 (2017).
12. Rivnay, J. *et al.* Organic electrochemical transistors. *Nat. Rev. Mater.* **3**, 17086 (2018).
13. Berggren, M. *et al.* Ion Electron–Coupled Functionality in Materials and Devices Based on Conjugated Polymers. *Adv. Mater.* **31**, 1805813 (2019).
14. Paulsen, B. D., Tybrandt, K., Stavrinidou, E. & Rivnay, J. Organic mixed ionic–electronic conductors. *Nat. Mater.* (2019)
15. Simon, D. T., Gabrielsson, E. O., Tybrandt, K. & Berggren, M. Organic Bioelectronics: Bridging the Signaling Gap between Biology and Technology. *Chem. Rev.* **116**, 13009–13041 (2016).
16. Zeglio, E., Rutz, A. L., Winkler, T. E., Malliaras, G. G. & Herland, A. Conjugated Polymers for Assessing and Controlling Biological Functions. *Adv. Mater.* **31**, 1806712 (2019).
17. Zeglio, E. & Inganäs, O. Active Materials for Organic Electrochemical Transistors. *Adv. Mater.* **30**, 1800941 (2018).
18. Moser, M., Ponder, J. F., Wadsworth, A., Giovannitti, A. & McCulloch, I. Materials in Organic Electrochemical Transistors for Bioelectronic Applications: Past, Present, and Future. *Adv. Funct. Mater.* 1807033 (2018)
19. Inal, S., Rivnay, J., Suiu, A. O., Malliaras, G. G. & McCulloch, I. Conjugated Polymers in Bioelectronics. *Acc. Chem. Res.* **51**, 1368–1376 (2018).
20. Larsson, K. C., Kjäll, P. & Richter-Dahlfors, A. Organic bioelectronics for electronic-to-chemical translation in modulation of neuronal signaling and machine-to-brain interfacing. *Biochim. Biophys. Acta BBA - Gen. Subj.* **1830**, 4334–4344 (2013).
21. Malliaras, G. G. Organic bioelectronics: A new era for organic electronics. *Biochim. Biophys. Acta BBA - Gen. Subj.* **1830**, 4286–4287 (2013).
22. Rivnay, J., Owens, R. M. & Malliaras, G. G. The Rise of Organic Bioelectronics. *Chem. Mater.* **26**, 679–685 (2014).

23. Burgt, Y. van de, Melianas, A., Keene, S. T., Malliaras, G. & Salleo, A. Organic electronics for neuromorphic computing. *Nat. Electron.* **1**, 386–397 (2018).
24. Fuller, E. J. *et al.* Parallel programming of an ionic floating-gate memory array for scalable neuromorphic computing. *Science* **364**, 570–574 (2019).
25. Brédas, J. L., Calbert, J. P., da Silva Filho, D. A. & Cornil, J. Organic semiconductors: a theoretical characterization of the basic parameters governing charge transport. *Proc. Natl. Acad. Sci. U. S. A.* **99**, 5804–9 (2002).
26. Coropceanu, V. *et al.* Charge Transport in Organic Semiconductors. *Chem. Rev.* **107**, 926–952 (2007).
27. Mas-Torrent, M. & Rovira, C. Role of Molecular Order and Solid-State Structure in Organic Field-Effect Transistors. *Chem. Rev.* **111**, 4833–4856 (2011).
28. Martinez, C. R. & Iverson, B. L. Rethinking the term “pi-stacking”. *Chem. Sci.* **3**, 2191 (2012).
29. Wang, C., Dong, H., Jiang, L. & Hu, W. Organic semiconductor crystals. *Chem. Soc. Rev.* **47**, 422–500 (2018).
30. Podzorov, V. Organic single crystals: Addressing the fundamentals of organic electronics. *MRS Bull.* **38**, 15–24 (2013).
31. Stingelin, N. On the phase behaviour of organic semiconductors. *Polym. Int.* **61**, 866–873 (2012).
32. Diao, Y., Shaw, L., Bao, Z. & B. Mannsfeld, S. C. Morphology control strategies for solution-processed organic semiconductor thin films. *Energy Environ. Sci.* **7**, 2145–2159 (2014).
33. Osaka, I. & McCullough, R. D. Advances in Molecular Design and Synthesis of Regioregular Polythiophenes. *Acc. Chem. Res.* **41**, 1202–1214 (2008).
34. Beaujuge, P. M. & Fréchet, J. M. J. Molecular Design and Ordering Effects in  $\pi$ -Functional Materials for Transistor and Solar Cell Applications. *J. Am. Chem. Soc.* **133**, 20009–20029 (2011).
35. Henson, Z. B., Müllen, K. & Bazan, G. C. Design strategies for organic semiconductors beyond the molecular formula. *Nat. Chem.* **4**, 699–704 (2012).
36. Mei, J., Diao, Y., Appleton, A. L., Fang, L. & Bao, Z. Integrated Materials Design of Organic Semiconductors for Field-Effect Transistors. *J. Am. Chem. Soc.* **135**, 6724–6746 (2013).
37. Yan, C. *et al.* Non-fullerene acceptors for organic solar cells. *Nat. Rev. Mater.* **3**, 18003 (2018).
38. Rivnay, J., Noriega, R., Kline, R. J., Salleo, A. & Toney, M. F. Quantitative analysis of lattice disorder and crystallite size in organic semiconductor thin films. *Phys. Rev. B* **84**, 045203 (2011).
39. DeLongchamp, D. M., Kline, R. J., Fischer, D. A., Richter, L. J. & Toney, M. F. Molecular Characterization of Organic Electronic Films. *Adv. Mater.* **23**, 319–337 (2011).
40. Rivnay, J., Mannsfeld, S. C. B., Miller, C. E., Salleo, A. & Toney, M. F. Quantitative determination of organic semiconductor microstructure from the molecular to device scale. *Chem. Rev.* **112**, 5488–5519 (2012).
41. Newbloom, G. M., Kanekal, K., Richards, J. J. & Pozzo, L. D. Section II: Microstructure of Semiconducting Polymers Chapter 5: Characterization of Polymer Semiconductors by Neutron Scattering Techniques. in *Semiconducting Polymers* 163–186 (2016).

42. Cavaye, H. Neutron Spectroscopy: An Under-Utilised Tool for Organic Electronics Research? *Angew. Chem. Int. Ed.* **58**, 9338–9346 (2019).
43. Urban, K. W. Studying Atomic Structures by Aberration-Corrected Transmission Electron Microscopy. *Science* **321**, 506–510 (2008).
44. Panova, O. *et al.* Diffraction imaging of nanocrystalline structures in organic semiconductor molecular thin films. *Nat. Mater.* **1** (2019)
45. Takacs, C. J., Brady, M. A., Treat, N. D., Kramer, E. J. & Chabinyc, M. L. Quadrites and crossed-chain crystal structures in polymer semiconductors. *Nano Lett.* **14**, 3096–3101 (2014).
46. Ewbank, P. C. *et al.* Synthesis, Characterization and Properties of Regioregular Polythiophene-Based Materials. in *Handbook of Thiophene-Based Materials* 157–217 (John Wiley & Sons, Ltd, 2009).
47. Warr, D. A. *et al.* Sequencing conjugated polymers by eye. *Sci. Adv.* **4**, eaas9543 (2018).
48. Hansen, M. R., Graf, R. & Spiess, H. W. Solid-State NMR in Macromolecular Systems: Insights on How Molecular Entities Move. *Acc. Chem. Res.* **46**, 1996–2007 (2013).
49. Hansen, M. R., Graf, R. & Spiess, H. W. Interplay of Structure and Dynamics in Functional Macromolecular and Supramolecular Systems As Revealed by Magnetic Resonance Spectroscopy. *Chem. Rev.* **116**, 1272–1308 (2016).
50. Snyder, C. R., DeLongchamp, D. M., Nieuwendaal, R. C. & Herzing, A. A. Chapter 7. Structure and Order in Organic Semiconductors. in *Polymer Chemistry Series* (ed. Luscombe, C.) 219–274 (Royal Society of Chemistry, 2016).
51. Spiess, H. W. 50th Anniversary Perspective: The Importance of NMR Spectroscopy to Macromolecular Science. *Macromolecules* **50**, 1761–1777 (2017).
52. Nieuwendaal, R. Chapter 15. Solid-state NMR of Organic Electronics. in *NMR Methods for Characterization of Synthetic and Natural Polymers* (eds. Zhang, R., Miyoshi, T. & Sun, P.) 325–362 (Royal Society of Chemistry, 2019).
53. Selter, P. & Hansen, M. R. Chapter 16. Molecular Chain Packing and Conformation in  $\pi$ -Conjugated Polymers from Solid-state NMR. in *NMR Methods for Characterization of Synthetic and Natural Polymers* (eds. Zhang, R., Miyoshi, T. & Sun, P.) 363–386 (Royal Society of Chemistry, 2019).
54. Mehring, M. *High Resolution NMR Spectroscopy in Solids*. (Springer-Verlag, 1976).
55. Street, G. B. & Clarke, T. C. Conducting Polymers: A Review of Recent Work. *IBM J. Res. Dev.* **25**, 51–57 (1981).
56. Schmidt-Rohr, K. & Spiess, H. W. *Multidimensional Solid-State NMR and Polymers*. (1994).
57. Duer, M. J. *Introduction to Solid-State NMR Spectroscopy*. (Wiley-Blackwell, 2005).
58. Levitt, M. H. *Spin Dynamics: Basics of Nuclear Magnetic Resonance*. (2008).
59. Hadgkinson, P. *Modern Methods in Solid-state NMR*. (2018).
60. Oganov, A. R., Pickard, C. J., Zhu, Q. & Needs, R. J. Structure prediction drives materials discovery. *Nat. Rev. Mater.* **4**, 331–348 (2019).
61. Brouwer, D. H. *et al.* A General Protocol for Determining the Structures of Molecularly Ordered but Noncrystalline Silicate Frameworks. *J. Am. Chem. Soc.* **135**, 5641–5655 (2013).
62. Dudenko, D. *et al.* A Strategy for Revealing the Packing in Semicrystalline  $\pi$ -Conjugated Polymers: Crystal Structure of Bulk Poly-3-hexyl-thiophene (P3HT). *Angew. Chem. Int. Ed.* **51**, 11068–11072 (2012).

63. Pickard, C. J., Salager, E., Pintacuda, G., Elena, B. & Emsley, L. Resolving Structures from Powders by NMR Crystallography Using Combined Proton Spin Diffusion and Plane Wave DFT Calculations. *J. Am. Chem. Soc.* **129**, 8932–8933 (2007).
64. Bryce, D. L. NMR crystallography: structure and properties of materials from solid-state nuclear magnetic resonance observables. *IUCrJ* **4**, 350–359 (2017).
65. Suzuki, F., Fukushima, T., Fukuchi, M. & Kaji, H. Refined Structure Determination of Blue-Emitting Tris(8-hydroxyquinoline) Aluminum(III) (Alq3) by the Combined Use of Cross-Polarization/Magic-Angle Spinning <sup>13</sup>C Solid-State NMR and First-Principles Calculation. *J. Phys. Chem. C* **117**, 18809–18817 (2013).
66. Olivier, Y. *et al.* 25th Anniversary Article: High-Mobility Hole and Electron Transport Conjugated Polymers: How Structure Defines Function. *Adv. Mater.* **26**, 2119–2136 (2014).
67. Chaudhari, S. R. *et al.* Donor–acceptor stacking arrangements in bulk and thin-film high-mobility conjugated polymers characterized using molecular modelling and MAS and surface-enhanced solid-state NMR spectroscopy. *Chem. Sci.* **8**, 3126–3136 (2017).
68. Brus, J. *et al.* Efficient Strategy for Determining the Atomic-Resolution Structure of Micro- and Nanocrystalline Solids within Polymeric Microbeads: Domain-Edited NMR Crystallography. *Macromolecules* **51**, 5364–5374 (2018).
69. Gélinas, S. *et al.* Ultrafast Long-Range Charge Separation in Organic Semiconductor Photovoltaic Diodes. *Science* **343**, 512–516 (2014).
70. Bredas, J.-L. When Electrons Leave Holes in Organic Solar Cells. *Science* **343**, 492–493 (2014).
71. Hinderberger, D. EPR Spectroscopy in Polymer Science. in *EPR Spectroscopy: Applications in Chemistry and Biology* (eds. Drescher, M. & Jeschke, G.) 67–89 (Springer, 2012).
72. Niklas, J. & Poluektov, O. G. Charge Transfer Processes in OPV Materials as Revealed by EPR Spectroscopy. *Adv. Energy Mater.* **7**, 1602226 (2017).
73. Biskup, T. Structure–Function Relationship of Organic Semiconductors: Detailed Insights From Time-Resolved EPR Spectroscopy. *Front. Chem.* **7**, (2019).
74. Palkovic, S. D. *et al.* Roadmap across the mesoscale for durable and sustainable cement paste – A bioinspired approach. *Constr. Build. Mater.* **115**, 13–31 (2016).
75. Liu, Y. *et al.* Application of anisotropic NMR parameters to the confirmation of molecular structure. *Nat. Protoc.* **14**, 217–247 (2019).
76. Tonelli, A. E. & Schilling, F. C. Carbon-13 NMR chemical shifts and the microstructure of polymers. *Acc. Chem. Res.* **14**, 233–238 (1981).
77. Born, R. & Spiess, H. W. Conformational Effects and Configurational Splitting in <sup>13</sup>C NMR Spectra of Synthetic Polymers As Investigated by ab Initio Individual Gauges for Localized Molecular Orbitals (IGLO) Calculations. *Macromolecules* **28**, 7785–7795 (1995).
78. Melnyk, A. *et al.* Macroscopic Structural Compositions of  $\pi$ -Conjugated Polymers: Combined Insights from Solid-State NMR and Molecular Dynamics Simulations. *J. Phys. Chem. Lett.* **8**, 4155–4160 (2017).
79. Snyder, C. R. *et al.* Quantifying Crystallinity in High Molar Mass Poly(3-hexylthiophene). *Macromolecules* **47**, 3942–3950 (2014).
80. Yuan, Y. *et al.* Multiple Chain Packing and Phase Composition in Regioregular Poly(3-butylthiophene) Films. *Macromolecules* **49**, 9493–9506 (2016).

81. Nieuwendaal, R. C., Snyder, C. R. & DeLongchamp, D. M. Measuring Order in Regioregular Poly(3-hexylthiophene) with Solid-State  $^{13}\text{C}$  CPMAS NMR. *ACS Macro Lett.* **3**, 130–135 (2014).
82. Shen, X., Hu, W. & Russell, T. P. Measuring the Degree of Crystallinity in Semicrystalline Regioregular Poly(3-hexylthiophene). *Macromolecules* **49**, 4501–4509 (2016).
83. Karki, A. *et al.* Unifying Energetic Disorder from Charge Transport and Band Bending in Organic Semiconductors. *Adv. Funct. Mater.* **29**, 1901109 (2019).
84. Noriega, R. *et al.* A general relationship between disorder, aggregation and charge transport in conjugated polymers. *Nat. Mater.* **12**, 1038–1044 (2013).
85. Parmer, J. E. *et al.* Organic bulk heterojunction solar cells using poly(2,5-bis(3-tetradecylthiophen-2-yl)thieno[3,2,-b]thiophene). *Appl. Phys. Lett.* **92**, 113309 (2008).
86. F. Hoefler, S. *et al.* The effect of polymer molecular weight on the performance of PTB7-Th:O-IDTBR non-fullerene organic solar cells. *J. Mater. Chem. A* **6**, 9506–9516 (2018).
87. Hamadani, B. H., Gundlach, D. J., McCulloch, I. & Heeney, M. Undoped polythiophene field-effect transistors with mobility of  $1\text{cm}^2\text{V}^{-1}\text{s}^{-1}$ . *Appl. Phys. Lett.* **91**, 243512 (2007).
88. Kolodziejcki, W. & Klinowski, J. Kinetics of Cross-Polarization in Solid-State NMR: A Guide for Chemists. *Chem. Rev.* **102**, 613–628 (2002).
89. Wu, C. H., Ramamoorthy, A. & Opella, S. J. High-Resolution Heteronuclear Dipolar Solid-State NMR Spectroscopy. *J. Magn. Reson. A* **109**, 270–272 (1994).
90. De Paëpe, G. *et al.* Transverse Dephasing Optimized Solid-State NMR Spectroscopy. *J. Am. Chem. Soc.* **125**, 13938–13939 (2003).
91. Andrew, E. R., Richards, R. E. & Packer, K. J. Magic angle spinning in solid state n.m.r. spectroscopy. *Philos. Trans. R. Soc. Lond. Ser. Math. Phys. Sci.* **299**, 505–520 (1981).
92. Kaji, H., Kusaka, Y., Onoyama, G. & Horii, F. CP/MAS  $^{13}\text{C}$  NMR Characterization of the Isomeric States and Intermolecular Packing in Tris(8-hydroxyquinoline) Aluminum(III) (Alq3). *J. Am. Chem. Soc.* **128**, 4292–4297 (2006).
93. Nishiyama, Y. *et al.* Characterization of local structures in amorphous and crystalline tris(8-hydroxyquinoline) aluminum(III) (Alq3) by solid-state  $^{27}\text{Al}$  MQMAS NMR spectroscopy. *Chem. Phys. Lett.* **471**, 80–84 (2009).
94. Beaujuge, P. M. *et al.* Synthetic Principles Directing Charge Transport in Low-Band-Gap Dithienosilole–Benzothiadiazole Copolymers. *J. Am. Chem. Soc.* **134**, 8944–8957 (2012).
95. Lemaur, V. *et al.* On the Supramolecular Packing of High Electron Mobility Naphthalene Diimide Copolymers: The Perfect Registry of Asymmetric Branched Alkyl Side Chains. *Macromolecules* **46**, 8171–8178 (2013).
96. Niedzialek, D. *et al.* Probing the relation between charge transport and supramolecular organization down to ångström resolution in a benzothiadiazole-cyclopentadithiophene copolymer. *Adv. Mater. Deerfield Beach Fla* **25**, 1939–47 (2013).
97. Pisula, W. *et al.* Solid-State Organization and Ambipolar Field-Effect Transistors of Benzothiadiazole-Cyclopentadithiophene Copolymer with Long Branched Alkyl Side Chains. *Polymers* **5**, 833–846 (2013).
98. Do, K. *et al.* Impact of Fluorine Substituents on  $\pi$ -Conjugated Polymer Main-Chain Conformations, Packing, and Electronic Couplings. *Adv. Mater.* **28**, 8197–8205 (2016).
99. Bohle, A. *et al.* A Generalized Packing Model for Bulk Crystalline Regioregular Poly(3-alkylthiophenes) with Extended Side Chains. *Macromol. Chem. Phys.* **219**, 1700266 (2018).

100. Lo, C. K. *et al.* Every Atom Counts: Elucidating the Fundamental Impact of Structural Change in Conjugated Polymers for Organic Photovoltaics. *Chem. Mater.* **30**, 2995–3009 (2018).
101. Brinkmann, M. *et al.* Correlation between Molecular Packing and Optical Properties in Different Crystalline Polymorphs and Amorphous Thin Films of mer-Tris(8-hydroxyquinoline)aluminum(III). *J. Am. Chem. Soc.* **122**, 5147–5157 (2000).
102. Amati, M. & Lelj, F. Luminescent Compounds fac- and mer-Aluminum Tris(quinolin-8-olate). A Pure and Hybrid Density Functional Theory and Time-Dependent Density Functional Theory Investigation of Their Electronic and Spectroscopic Properties. *J. Phys. Chem. A* **107**, 2560–2569 (2003).
103. Baldacchini, G., Chiacchiaretta, P., Reisfeld, R. & Zigansky, E. The origin of luminescence blueshifts in Alq3 composites. *J. Lumin.* **129**, 1849–1852 (2009).
104. Tsuboi, T. & Torii, Y. Photoluminescence characteristics of green and blue emitting Alq3 organic molecules in crystals and thin films. *J. Non-Cryst. Solids* **356**, 2066–2069 (2010).
105. Bi, H. *et al.* Fac-Alq3 and Mer-Alq3 Nano/Microcrystals with Different Emission and Charge-Transporting Properties. *Adv. Mater.* **22**, 1631–1634 (2010).
106. Bi, H. *et al.* A green emissive amorphous fac-Alq3 solid generated by grinding crystalline blue fac-Alq3 powder. *Chem. Commun.* **47**, 4135–4137 (2011).
107. Muccini, M. *et al.* Blue Luminescence of Facial Tris(quinolin-8-olato)aluminum(III) in Solution, Crystals, and Thin Films. *Adv. Mater.* **16**, 861–864 (2004).
108. Cölle, M., Dinnebir, R. E. & Brütting, W. The structure of the blue luminescent  $\delta$ -phase of tris(8-hydroxyquinoline)aluminium(III) (Alq3). *Chem. Commun.* 2908–2909 (2002)
109. Kaji, H., Kusaka, Y., Onoyama, G. & Horii, F. Relationships between Light-Emitting Properties and Different Isomers in Polymorphs of Tris(8-hydroxyquinoline) Aluminum(III) (Alq3) Analyzed by Solid-State  $^{27}\text{Al}$  NMR and Density Functional Theory (DFT) Calculations. *Jpn. J. Appl. Phys.* **44**, 3706 (2005).
110. Nandagopal, M., Mathai, M., Papadimitrakopoulos, F. & Utz, M. NMR of Organic Semiconductors. in *Modern Magnetic Resonance* (ed. Webb, G. A.) 1539–1545 (Springer Netherlands, 2006).
111. Goswami, M., Nayak, P. K., Periasamy, N. & Madhu, P. Characterisation of different polymorphs of tris(8-hydroxyquinolinato)aluminium(III) using solid-state NMR and DFT calculations. *Chem. Cent. J.* **3**, 15 (2009).
112. Luzio, A. *et al.* Microstructural control suppresses thermal activation of electron transport at room temperature in polymer transistors. *Nat. Commun.* **10**, 3365 (2019).
113. Stalder, R. *et al.* Ambipolar Charge Transport in Isoindigo-Based Donor–Acceptor Polymers. *Chem. Mater.* **28**, 1286–1297 (2016).
114. Rankin, A. G. M., Trébos, J., Pourpoint, F., Amoureux, J.-P. & Lafon, O. Recent developments in MAS DNP-NMR of materials. *Solid State Nucl. Magn. Reson.* **101**, 116–143 (2019).
115. Lilly Thankamony, A. S., Wittmann, J. J., Kaushik, M. & Corzilius, B. Dynamic nuclear polarization for sensitivity enhancement in modern solid-state NMR. *Prog. Nucl. Magn. Reson. Spectrosc.* **102–103**, 120–195 (2017).
116. Rossini, A. J. *et al.* Dynamic Nuclear Polarization Surface Enhanced NMR Spectroscopy. *Acc. Chem. Res.* **46**, 1942–1951 (2013).
117. Barnes, A. B. *et al.* High-Field Dynamic Nuclear Polarization for Solid and Solution Biological NMR. *Appl. Magn. Reson.* **34**, 237–263 (2008).

118. Clauss, J., Schmidt-Rohr, K. & Spiess, H. W. Determination of domain sizes in heterogeneous polymers by solid-state NMR. *Acta Polym.* **44**, 1–17 (1993).
119. Schlagnitweit, J. *et al.* A solid-state NMR method to determine domain sizes in multi-component polymer formulations. *J. Magn. Reson.* **261**, 43–48 (2015).
120. Nieuwendaal, R. C. *et al.* Measuring domain sizes and compositional heterogeneities in P3HT-PCBM bulk heterojunction thin films with <sup>1</sup>H spin diffusion NMR spectroscopy. *Adv. Funct. Mater.* **22**, 1255–1266 (2012).
121. Etzold, F. *et al.* Sub-ns triplet state formation by non-geminate recombination in PSBTBT:PC 70 BM and PCPDTBT:PC 60 BM organic solar cells. *Energy Environ. Sci.* **8**, 1511–1522 (2015).
122. Heeger, A. J. 25th Anniversary Article: Bulk Heterojunction Solar Cells: Understanding the Mechanism of Operation. *Adv. Mater.* **26**, 10–28 (2014).
123. Gasparini, N., Salleo, A., McCulloch, I. & Baran, D. The role of the third component in ternary organic solar cells. *Nat. Rev. Mater.* (2019)
124. Zalar, P., Henson, Z. B., Welch, G. C., Bazan, G. C. & Nguyen, T. Q. Color tuning in polymer light-emitting diodes with lewis acids. *Angew. Chem. - Int. Ed.* **51**, 7495–7498 (2012).
125. Wang, Z. *et al.* The Role of Weak Molecular Dopants in Enhancing the Performance of Solution-Processed Organic Field-Effect Transistors. *Adv. Electron. Mater.* **5**, 1800547 (2019).
126. Lüssem, B. *et al.* Doped Organic Transistors. *Chem. Rev.* **116**, 13714–13751 (2016).
127. Zhang, G. *et al.* Nonfullerene Acceptor Molecules for Bulk Heterojunction Organic Solar Cells. *Chem. Rev.* **118**, 3447–3507 (2018).
128. Lu, L. *et al.* Recent Advances in Bulk Heterojunction Polymer Solar Cells. *Chem. Rev.* **115**, 12666–12731 (2015).
129. Lüssem, B., Riede, M. & Leo, K. Doping of organic semiconductors. *Phys. Status Solidi A* **210**, 9–43 (2013).
130. Reineke, S. & Baldo, M. A. Recent progress in the understanding of exciton dynamics within phosphorescent OLEDs. *Phys. Status Solidi A* **209**, 2341–2353 (2012).
131. Salzmann, I., Heimel, G., Oehzelt, M., Winkler, S. & Koch, N. Molecular Electrical Doping of Organic Semiconductors: Fundamental Mechanisms and Emerging Dopant Design Rules. *Acc. Chem. Res.* **49**, 370–378 (2016).
132. Street, R. A. Electronic Structure and Properties of Organic Bulk-Heterojunction Interfaces. *Adv. Mater.* **28**, 3814–3830 (2016).
133. Burke, T. M., Sweetnam, S., Vandewal, K. & McGehee, M. D. Beyond Langevin Recombination: How Equilibrium Between Free Carriers and Charge Transfer States Determines the Open-Circuit Voltage of Organic Solar Cells. *Adv. Energy Mater.*
134. Vandewal, K. Interfacial Charge Transfer States in Condensed Phase Systems. *Annu. Rev. Phys. Chem.* **67**, 113–133 (2016).
135. Lin, Y. L., Fusella, M. A. & Rand, B. P. The Impact of Local Morphology on Organic Donor/Acceptor Charge Transfer States. *Adv. Energy Mater.* **8**, 1702816 (2018).
136. Coropceanu, V., Chen, X.-K., Wang, T., Zheng, Z. & Brédas, J.-L. Charge-transfer electronic states in organic solar cells. *Nat. Rev. Mater.* (2019)
137. Karki, A. *et al.* Understanding the High Performance of over 15% Efficiency in Single-Junction Bulk Heterojunction Organic Solar Cells. *Adv. Mater.* **31**, 1903868 (2019).

138. Ryno, S. M., Ravva, M. K., Chen, X., Li, H. & Brédas, J.-L. Molecular Understanding of Fullerene – Electron Donor Interactions in Organic Solar Cells. *Adv. Energy Mater.* **7**, 1601370 (2017).
139. Graham, K. R. *et al.* Importance of the Donor:Fullerene Intermolecular Arrangement for High-Efficiency Organic Photovoltaics. *J. Am. Chem. Soc.* **136**, 9608–9618 (2014).
140. Miller, N. C. *et al.* Use of X-Ray Diffraction, Molecular Simulations, and Spectroscopy to Determine the Molecular Packing in a Polymer-Fullerene Bimolecular Crystal. *Adv. Mater.* **24**, 6071–6079 (2012).
141. Nieuwendaal, R. C. *et al.* Characterization of Interfacial Structure in Polymer-Fullerene Bulk Heterojunctions via  $^{13}\text{C}\{^2\text{H}\}$  Rotational Echo Double Resonance NMR. *Phys. Rev. Lett.* **121**, 026101 (2018).
142. Zhang, T. *et al.* Impact of side-chain length on the phase structures of P3ATs and P3AT:PCBM films as revealed by SSNMR and FTIR. *J. Polym. Sci. Part B Polym. Phys.* (2018)
143. Wang, C. *et al.* Intermolecular Arrangement of Fullerene Acceptors Proximal to Semiconducting Polymers in Mixed Bulk Heterojunctions. *Angew. Chem. Int. Ed.* **57**, 7034–7039 (2018).
144. Etzold, F. *et al.* The Effect of Solvent Additives on Morphology and Excited-State Dynamics in PCPDTBT:PCBM Photovoltaic Blends. *J. Am. Chem. Soc.* **134**, 10569–10583 (2012).
145. Lee, J. K. *et al.* Processing Additives for Improved Efficiency from Bulk Heterojunction Solar Cells. *J. Am. Chem. Soc.* **130**, 3619–3623 (2008).
146. Liao, H.-C. *et al.* Additives for morphology control in high-efficiency organic solar cells. *Mater. Today* **16**, 326–336 (2013).
147. McDowell, C., Abdelsamie, M., Toney, M. F. & Bazan, G. C. Solvent Additives: Key Morphology-Directing Agents for Solution-Processed Organic Solar Cells. *Adv. Mater.* **30**, 1707114 (2018).
148. Perez, L. a *et al.* Solvent additive effects on small molecule crystallization in bulk heterojunction solar cells probed during spin casting. *Adv. Mater. Deerfield Beach Fla* **25**, 6380–4 (2013).
149. Sharenko, A., Gehrig, D., Laquai, F. & Nguyen, T.-Q. The Effect of Solvent Additive on the Charge Generation and Photovoltaic Performance of a Solution-Processed Small Molecule:Perylene Diimide Bulk Heterojunction Solar Cell. *Chem. Mater.* **26**, 4109–4118 (2014).
150. Abate, A. *et al.* Lithium salts as “redox active” p-type dopants for organic semiconductors and their impact in solid-state dye-sensitized solar cells. *Phys. Chem. Chem. Phys.* **15**, 2572–2579 (2013).
151. Cochran, J. E. *et al.* Molecular Interactions and Ordering in Electrically Doped Polymers: Blends of PBTTT and F<sub>4</sub>TCNQ. *Macromolecules* **47**, 6836–6846 (2014).
152. Yurash, B. *et al.* Atomic-Level Insight into the Postsynthesis Band Gap Engineering of a Lewis Base Polymer Using Lewis Acid Tris(pentafluorophenyl)borane. *Chem. Mater.* **31**, 6715–6725 (2019).
153. Hynynen, J. *et al.* Enhanced Electrical Conductivity of Molecularly p-Doped Poly(3-hexylthiophene) through Understanding the Correlation with Solid-State Order. *Macromolecules* **50**, 8140–8148 (2017).

154. Hamidi-Sakr, A. *et al.* A Versatile Method to Fabricate Highly In-Plane Aligned Conducting Polymer Films with Anisotropic Charge Transport and Thermoelectric Properties: The Key Role of Alkyl Side Chain Layers on the Doping Mechanism. *Adv. Funct. Mater.* **27**, 1700173 (2017).
155. McCulloch, I. *et al.* Liquid-crystalline semiconducting polymers with high charge-carrier mobility. *Nat. Mater.* **5**, 328–333 (2006).
156. Schuettfort, T. *et al.* Microstructure of Polycrystalline PBTTT Films: Domain Mapping and Structure Formation. *ACS Nano* **6**, 1849–1864 (2012).
157. Chabinyk, M. L., Toney, M. F., Kline, R. J., McCulloch, I. & Heeney, M. X-ray Scattering Study of Thin Films of Poly(2,5-bis(3-alkylthiophen-2-yl)thieno[3,2-b]thiophene). *J. Am. Chem. Soc.* **129**, 3226–3237 (2007).
158. Cho, E. *et al.* Three-Dimensional Packing Structure and Electronic Properties of Biaxially Oriented Poly(2,5-bis(3-alkylthiophene-2-yl)thieno[3,2-b]thiophene) Films. *J. Am. Chem. Soc.* **134**, 6177–6190 (2012).
159. Brocorens, P. *et al.* Solid-State Supramolecular Organization of Polythiophene Chains Containing Thienothiophene Units. *Adv. Mater.* **21**, 1193–1198 (2009).
160. Vakhshouri, K. & Gomez, E. D. Effect of Crystallization Kinetics on Microstructure and Charge Transport of Polythiophenes. *Macromol. Rapid Commun.* **33**, 2133–2137 (2012).
161. Yazawa, K., Inoue, Y., Yamamoto, T. & Asakawa, N. Twist glass transition in regioregulated poly(3-alkylthiophene). *Phys. Rev. B* **74**, 094204 (2006).
162. Yazawa, K., Inoue, Y., Shimizu, T., Tansho, M. & Asakawa, N. Molecular Dynamics of Regioregular Poly(3-hexylthiophene) Investigated by NMR Relaxation and an Interpretation of Temperature Dependent Optical Absorption. *J. Phys. Chem. B* **114**, 1241–1248 (2010).
163. Martini, F. *et al.* P3HT/PCBM Photoactive Materials for Solar Cells: Morphology and Dynamics by Means of Solid-State NMR. *J. Phys. Chem. C* **117**, 131–139 (2013).
164. Zhan, P. *et al.* Side chain length affects backbone dynamics in poly(3-alkylthiophene)s. *J. Polym. Sci. Part B Polym. Phys.* **56**, 1193–1202 (2018).
165. Chung, H. *et al.* Rotator side chains trigger cooperative transition for shape and function memory effect in organic semiconductors. *Nat. Commun.* **9**, 1–12 (2018).
166. Reddy, G. N. M. *et al.* Co-existence of Distinct Supramolecular Assemblies in Solution and in the Solid State. *Chem. – Eur. J.* **23**, 2315–2322 (2017).
167. Shu, J. *et al.* Coexistence of Helical Morphologies in Columnar Stacks of Star-Shaped Discotic Hydrazones. *J. Am. Chem. Soc.* **135**, 11075–11086 (2013).
168. Reddy G. N. M., Ballesteros-Garrido, R., Lacour, J. & Caldarelli, S. Determination of Labile Chiral Supramolecular Ion Pairs by Chromatographic NMR Spectroscopy. *Angew. Chem. Int. Ed.* **52**, 3255–3258 (2013).
169. Herkert, L. *et al.* Pathway Control in Cooperative vs. Anti-Cooperative Supramolecular Polymers. *Angew. Chem. Int. Ed.* **58**, 11344–11349 (2019).
170. Langenstroer, A. *et al.* Unraveling Concomitant Packing Polymorphism in Metallosupramolecular Polymers. *J. Am. Chem. Soc.* **141**, 5192–5200 (2019).
171. Wolf, J. *et al.* Benzo[1,2-b:4,5-b']dithiophene–Pyrido[3,4-b]pyrazine Small-Molecule Donors for Bulk Heterojunction Solar Cells. *Chem. Mater.* **28**, 2058–2066 (2016).
172. Wang, K. *et al.* Donor and Acceptor Unit Sequences Influence Material Performance in Benzo[1,2-b:4,5-b']dithiophene–6,7-Difluoroquinoxaline Small Molecule Donors for BHJ Solar Cells. *Adv. Funct. Mater.* **26**, 7103–7114 (2016).

173. Shaibat, M. A., Casabianca, L. B., Siberio-Pérez, D. Y., Matzger, A. J. & Ishii, Y. Distinguishing Polymorphs of the Semiconducting Pigment Copper Phthalocyanine by Solid-State NMR and Raman Spectroscopy. *J. Phys. Chem. B* **114**, 4400–4406 (2010).
174. Zhou, C. *et al.* Topological Transformation of  $\pi$ -Conjugated Molecules Reduces Resistance to Crystallization. *Angew. Chem. Int. Ed.* **56**, 9318–9321 (2017).
175. Seifrid, M. T., Reddy, G. N. M., Zhou, C., Chmelka, B. F. & Bazan, G. C. Direct Observation of the Relationship Between Molecular Topology and Bulk Morphology for a  $\pi$ -Conjugated Material. *J. Am. Chem. Soc.* **141**, 5078–5082 (2019).
176. Suzuki, K. *et al.* Analysis of Molecular Orientation in Organic Semiconducting Thin Films Using Static Dynamic Nuclear Polarization Enhanced Solid-State NMR Spectroscopy. *Angew. Chem. Int. Ed.* **56**, 14842–14846 (2017).
177. Street, R. A. Unraveling Charge Transport in Conjugated Polymers. *Science* **341**, 1072–1073 (2013).
178. Zhang, X. *et al.* Molecular origin of high field-effect mobility in an indacenodithiophene–benzothiadiazole copolymer. *Nat. Commun.* **4**, 1–9 (2013).
179. Tsao, H. N. *et al.* Ultrahigh Mobility in Polymer Field-Effect Transistors by Design. *J. Am. Chem. Soc.* **133**, 2605–2612 (2011).
180. Griffin, J. M., Forse, A. C. & Grey, C. P. Solid-state NMR studies of supercapacitors. *Solid State Nucl. Magn. Reson.* **74–75**, 16–35 (2016).
181. Forse, A. C. *et al.* Direct observation of ion dynamics in supercapacitor electrodes using in situ diffusion NMR spectroscopy. *Nat. Energy* **2**, 1–7 (2017).
182. Forse, A. C., Merlet, C., Griffin, J. M. & Grey, C. P. New Perspectives on the Charging Mechanisms of Supercapacitors. *J. Am. Chem. Soc.* **138**, 5731–5744 (2016).
183. Witherspoon, V. J., Xu, J. & Reimer, J. A. Solid-State NMR Investigations of Carbon Dioxide Gas in Metal–Organic Frameworks: Insights into Molecular Motion and Adsorptive Behavior. *Chem. Rev.* **118**, 10033–10048 (2018).
184. Witherspoon, V. J. *et al.* Translational and Rotational Motion of C8 Aromatics Adsorbed in Isotropic Porous Media (MOF-5): NMR Studies and MD Simulations. *J. Phys. Chem. C* **121**, 15456–15462 (2017).
185. Forse, A. C. *et al.* Unexpected Diffusion Anisotropy of Carbon Dioxide in the Metal–Organic Framework Zn<sub>2</sub>(dobpdc). *J. Am. Chem. Soc.* **140**, 1663–1673 (2018).
186. Forse, A. C., Altobelli, S. A., Benders, S., Conradi, M. S. & Reimer, J. A. Revisiting Anisotropic Diffusion of Carbon Dioxide in the Metal–Organic Framework Zn<sub>2</sub>(dobpdc). *J. Phys. Chem. C* **122**, 15344–15351 (2018).
187. van der Wel, P. C. A. New applications of solid-state NMR in structural biology. *Emerg. Top. Life Sci.* **2**, 57–67 (2018).
188. Mandala, V. S., Williams, J. K. & Hong, M. Structure and Dynamics of Membrane Proteins from Solid-State NMR. *Annu. Rev. Biophys.* **47**, 201–222 (2018).
189. Knight, M. J. *et al.* Structure and backbone dynamics of a microcrystalline metalloprotein by solid-state NMR. *Proc. Natl. Acad. Sci.* **109**, 11095–11100 (2012).
190. Nishiyama, Y., Fukushima, T., Fukuchi, M., Fujimura, S. & Kaji, H. Sensitivity boosting in solid-state NMR of thin organic semiconductors by a paramagnetic dopant of copper phthalocyanine. *Chem. Phys. Lett.* **556**, 195–199 (2013).
191. Hou, H. *et al.* Conjugated oligoelectrolytes increase power generation in E. coli microbial fuel cells. *Adv. Mater. Deerfield Beach Fla* **25**, 1593–7 (2013).

192. Yan, H., Catania, C. & Bazan, G. C. Membrane-Intercalating Conjugated Oligoelectrolytes: Impact on Bioelectrochemical Systems. *Adv. Mater.* **27**, 2958–2973 (2015).
193. Garner, L. E., Thomas, A. W., Sumner, J. J., Harvey, S. P. & Bazan, G. C. Conjugated oligoelectrolytes increase current response and organic contaminant removal in wastewater microbial fuel cells. *Energy Environ. Sci.* **5**, 9449 (2012).
194. Herland, A. & Inganäs, O. Conjugated Polymers as Optical Probes for Protein Interactions and Protein Conformations. *Macromol. Rapid Commun.* **28**, 1703–1713 (2007).
195. Yuan, H., Wang, B., Lv, F., Liu, L. & Wang, S. Conjugated-Polymer-Based Energy-Transfer Systems for Antimicrobial and Anticancer Applications. *Adv. Mater.* **26**, 6978–6982 (2014).
196. Bryce, D. L. New frontiers for solid-state NMR across the periodic table: a snapshot of modern techniques and instrumentation. *Dalton Trans.* **48**, 8014–8020 (2019).
197. Chen, P. *et al.* Magic angle spinning spheres. *Sci. Adv.* **4**, eaau1540 (2018).
198. Samoson, A. H-MAS. *J. Magn. Reson.* **306**, 167–172 (2019).
199. Hong, Y., Manjunatha Reddy, G. N. & Nishiyama, Y. Selective detection of active pharmaceutical ingredients in tablet formulations using solid-state NMR spectroscopy. *Solid State Nucl. Magn. Reson.* 101651 (2020)
200. Lee, S. Sensitive detection of NMR for thin films. *Solid State Nucl. Magn. Reson.* **71**, 1–10 (2015).
201. Paruzzo, F. M. *et al.* Chemical shifts in molecular solids by machine learning. *Nat. Commun.* **9**, 1–10 (2018).